micromachines

MDPI

Review

Third-Order Optical Nonlinearities of 2D Materials at Telecommunications Wavelengths

Linnan Jia [1], Jiayang Wu [1,*], Yuning Zhang [1], Yang Qu [1], Baohua Jia [2,3] and David J. Moss [1,*]

[1] Optical Sciences Center, Swinburne University of Technology, Hawthorn, VIC 3122, Australia
[2] School of Science, RMIT University, Melbourne, VIC 3001, Australia
[3] Australian Research Council (ARC) Industrial Transformation Training, Centre in Surface Engineering for Advanced Materials (SEAM), RMIT University, Melbourne, VIC 3000, Australia
* Correspondence: jiayangwu@swin.edu.au (J.W.); dmoss@swin.edu.au (D.J.M.)

Abstract: All-optical signal processing based on nonlinear optical devices is promising for ultrafast information processing in optical communication systems. Recent advances in two-dimensional (2D) layered materials with unique structures and distinctive properties have opened up new avenues for nonlinear optics and the fabrication of related devices with high performance. This paper reviews the recent advances in research on third-order optical nonlinearities of 2D materials, focusing on all-optical processing applications in the optical telecommunications band near 1550 nm. First, we provide an overview of the material properties of different 2D materials. Next, we review different methods for characterizing the third-order optical nonlinearities of 2D materials, including the Z-scan technique, third-harmonic generation (THG) measurement, and hybrid device characterization, together with a summary of the measured n_2 values in the telecommunications band. Finally, the current challenges and future perspectives are discussed.

Keywords: third-order optical nonlinearity; 2D materials; telecommunications band

Citation: Jia, L.; Wu, J.; Zhang, Y.; Qu, Y.; Jia, B.; Moss, D.J. Third-Order Optical Nonlinearities of 2D Materials at Telecommunications Wavelengths. *Micromachines* **2023**, *14*, 307. https://doi.org/10.3390/mi14020307

Academic Editor: Eui-Hyeok Yang

Received: 25 December 2022
Revised: 14 January 2023
Accepted: 14 January 2023
Published: 25 January 2023

1. Introduction

All-optical signal processing based on nonlinear optical devices is an attractive technique for ultrahigh speed signal processing for optical communication systems. It offers broad operation bandwidths, ultra-high processing speeds, together with low power consumption and potentially reduced footprint and cost. Integrated nonlinear optical photonic chips have been based on a few key materials including silicon (Si) [1–3], doped silica (SiO_2) [4,5], silicon nitride (Si_3N_4) [6,7], aluminum gallium arsenide (AlGaAs) [8–10], and chalcogenide glasses [11,12]. These have enabled a wide range of devices from Raman amplification and lasing [13–15], wavelength conversion [5,12,16–18], optical logic gates [19–22], and optical frequency comb generation [23–26], to optical temporal cloaking [27], quantum entangling [28–30], and many others. Despite their success, no platform is perfect—they all have limitations, such as a relatively small Kerr nonlinearity (n_2) (e.g., for Si_3N_4) or high two photon absorption (for silicon in the telecommunications band), resulting in a low nonlinear figure of merit (FOM = $n_2/(\lambda\beta_{TPA})$, with n_2 and β_{TPA} denoting the effective Kerr coefficient and TPA coefficient of the waveguides, respectively, and λ the light wavelength).

To overcome these limitations, newly emerging materials have attracted significant attention, particularly 2D-layered materials, such as graphene [31–33], GO [34–36], TMDCs [37–40], h-BN [41–43], and BP [44–46], where their atomically thin nature yields unique and superior properties. Compared with bulk materials, the 2D materials possess surfaces that are free of dangling bonds due to their weak out-of-plane van der Waals interactions [32,37]. In particular, their properties are highly dependent on the number of atomic layers—not only is their optical bandgap highly layer thickness dependent but they can also exhibit an indirect-to-direct bandgap transition (and the reverse), which provides

powerful ways in which to tune their optical responses [37,46–48]. Further, their broadband photoluminescence and ultrahigh carrier mobility are highly attractive features for photonic and optoelectronic applications [33,49–53]. The unique photon-excited exciton and valley-selective properties of monolayer TMDCs and their heterostructures are promising for the development of future spintronic and quantum computing devices [37,38]. Finally, in addition to their linear optical properties, 2D materials exhibit remarkable nonlinear optical properties including strong saturable absorption (SA) [54–57], a giant Kerr nonlinearity [58–62], and prominent second- (SHG) and third-harmonic generation (THG) [44,63–65], opening up new avenues for high-performance nonlinear optical devices.

In contrast to the second-order optical nonlinearity that only exists in non-centrosymmetric materials, the third-order susceptibility is present in all materials, which gives rise to a rich variety of processes, including four-wave mixing (FWM), self-phase modulation (SPM), cross-phase modulation (XPM), THG, two-photon absorption (TPA), SA, stimulated Raman scattering, and many others. These third-order nonlinear optical processes are quasi-instantaneous with ultrafast response times on the order of femtoseconds [66]. This has motivated ultrafast all-optical signal generation and processing for telecommunications, spectroscopy, metrology, sensing, quantum optics, and many other areas [67,68].

In this paper, we review recent progress in the study of the third-order optical nonlinearities of 2D materials specifically in the telecommunications wavelength band near 1550 nm, in contrast with other reviews [44,69,70] that focus predominantly in the visible wavelength range. We discuss the different techniques for characterizing the third-order optical nonlinearity and the prospects for future development. In Section 2, the material properties of different 2D materials are briefly introduced and compared. Next, we review different methods used to characterize the third-order nonlinear optical response of 2D materials, including Z-scan technique, THG measurement, and hybrid device characterization. We also summarize the measured values of n_2 of different 2D materials in the telecommunications band. Finally, the conclusion and future perspectives are discussed in Section 4. Our review is aimed to help readers have a view of the progress in this field and to provide guidance for optimizing the properties and device applications of 2D materials in future optical telecommunications systems.

2. 2D Materials

The past decade has witnessed an enormous surge in research on layered 2D materials—many have been discovered and synthesized with a wide range of properties. In this section, we briefly introduce some key 2D materials such as graphene, GO, TMDCs, h-BN, and BP as shown in Figure 1 and discuss their electrical and optical properties.

2.1. Graphene and Graphene Oxide

Graphene, and its derivative, graphene oxide (GO), have been intensely studied due to their excellent mechanical, electrical, and optical properties [33,71,72]. Graphene has a gapless band structure, in which the conduction and valence bands meet at the K point of Brillouin zone, resulting in its semimetal nature [31,44,73]. In contrast, GO is an electronically hybrid material, featuring both conducting π-states from sp^2 carbon sites and a large energy gap between the σ-states of its sp^3-bonded carbons [34,74]. Their unique band structures result in novel electrical and optical properties, where for graphene, for example, the electrons and holes act as massless Dirac fermions resulting in extremely high carrier mobilities (>10^5 cm^2/Vs) even under ambient conditions [31]. In contrast, GO exhibits a band gap that is tunable by adjusting the degree of reduction, which in turn affects the electric and optical properties. In addition, GO exhibits fluorescence in the near-infrared (NIR), visible and ultraviolet regions [34–36], which is very promising for light emitting devices. Moreover, the excellent nonlinear optical properties of both materials have been reported, including strong saturable absorption (SA) [75,76], a giant optical Kerr nonlinearity [58,59], leading to efficient self-phase modulation [77], FWM [78,79], as well as high harmonic generation [63].

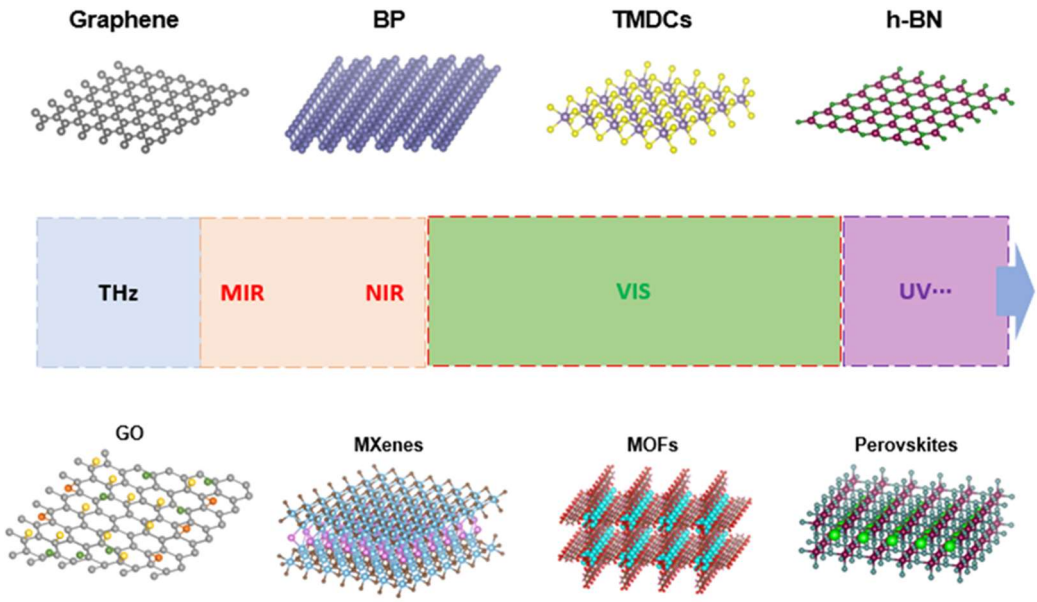

Figure 1. Illustration of typical 2D-layered materials.

2.2. Transition Metal Dichalcogenides

Transition metal dichalcogenides (TMDCs) with the formula of MX_2 (where M is a transition metal and X is a chalcogen), is another widely studied family of 2D materials. Different to the semimetal graphene, monolayer TMDCs, such as MoS_2, $MoSe_2$, WS_2, and WSe_2, are typically semiconductors that have bandgaps from 1 eV to 2.5 eV, covering the spectral range from the near infrared to the visible region [37,38]. Moreover, TMDCs can exhibit a transition from direct- to indirect-bandgaps with increasing film thickness, resulting in strongly thickness-tunable optical and electrical properties. For instance, MoS_2 exhibits layer-dependent photoluminescence, with monolayer films showing a much stronger photoluminescence [80]. Monolayer hexagonal TMDCs also exhibit unique band structure valley-dependent properties, such as valley coherence and valley-selective circular dichroism [37,81], offering new prospects for novel applications in optical computing and information processing. For the nonlinear optical properties, TMDCs with odd numbers of layers have no inversion symmetry, and so exhibit a non-zero second-order (and higher even-order) nonlinearities that are absent in graphene and even-layer TMDCs [44,64]. Recently, noble metal TMDCs, including $PdSe_2$ and $PtSe_2$, and $PdTe_2$, have also attracted increasing interest in the fabrication of high performance electronic and optical devices, such as ultra-broadband photodetectors [39,40] as well as mode-locked lasers [82].

2.3. Black Phosphorus

Black phosphorus (BP) is another attractive single element 2D-layered material which has been widely studied. It has a puckered crystal structure, yielding a strong in-plane anisotropy in its physical properties in the "armchair" and "zigzag" directions, opening new avenues for anisotropic electronic and optoelectronic devices [44,45,83]. Moreover, BP is a semiconductor that features a layer thickness-dependent direct bandgap from 0.3 eV (bulk) to 2.0 eV (monolayer), bridging the gap between the zero-bandgap graphene and large-bandgap TMDCs [48,83]. This broad bandgap tunability is very suitable for the photodetection and photonic applications from the visible to mid-infrared spectra regions [46,47,84]. For the nonlinear optical properties, the layer thickness tunable and polarization-dependent THG and optical Kerr nonlinearity have been demonstrated recently [83,85]. Broadband SA has also been observed in BP, demonstrating its strong potential for ultrafast pulsed lasers [86–88].

2.4. Other Emerging 2D Materials

A wide range of other novel 2D low-dimensional materials have been investigated, including h-BN, MXenes, perovskites, as well as MOFs, which greatly enriches the family of 2D materials. h-BN is an electrical insulator with a large bandgap of around 5.9 eV [41,89] making h-BN a candidate for ultraviolet light applications. It also has an ultra-flat surface as well as excellent resistance to oxidation and corrosion, which are both highly useful as a dielectric or capping layer to protect the active materials or devices from degradation [41].

MXenes belong to another family of 2D materials, including 2D transition metal carbides, nitrides, and carbonitrides. Typically, the electronic structure of MXenes can be tuned by varying the surface functional groups. For instance, nonterminated Ti_3C_2 theoretically resembles a typical semimetal with a finite density of states at the Fermi level, whereas it can transition to a semiconductor when terminated with surface groups, such as OH and F groups [90]. MXnens also exhibit superior optical properties, such as a high optical transmittance of visible light (>97% per nm) [38,91], and excellent nonlinear optical properties [57].

Organometal-halide perovskites have a general formula of ABX_3, where typically A = $CH_3NH_3^+$, B = Pb^{2+}, and X = I^-, Br^-, Cl^- or mixtures [92]. Due to their prominent photovoltaic features and luminescence properties, organometal-halide perovskite semiconductors have been widely used to design high performance solar cells as well as light-emitting diodes [51–53]. Metal-organic frameworks (MOFs) are organic–inorganic hybrid porous crystalline materials with metal ions or metal-oxo clusters coordinated with organic linkers [93,94]. Thanks to this unique structure, 2D MOFs exhibit enhanced photo-physical behaviour and are promising for various applications, from light emission and sensing to nonlinear optical applications [95,96].

3. Third-Order Optical Nonlinearities of 2D Materials in the Telecommunications Band

With their excellent third-order optical nonlinearities, 2D materials are promising functional materials for high-performance nonlinear optical devices. In this section, we review the different methods used to characterize their third-order nonlinear optical response. These include the Z-scan technique, THG measurement, and hybrid device characterization. We also summarize and compare the measured n_2 values of different 2D materials in the telecommunications band.

3.1. Third-Order Optical Nonlinearity

The nonlinear optical response of a material in the dipole approximation is given by [1,97]:

$$\widetilde{P}(t) = \varepsilon_0[\chi^{(1)}\cdot\widetilde{E}(t) + \chi^{(2)} \ : \ \widetilde{E}(t)\widetilde{E}(t) + \chi^{(3)}\vdots\ \widetilde{E}(t)\widetilde{E}(t)\widetilde{E}(t) + \dots\,] \quad (1)$$

where the $\widetilde{P}(t)$ is the material electronic polarization, $\widetilde{E}(t)$ is the incident field, $\chi^{(n)}$ are the n^{th}-order nonlinear optical susceptibility. The first-order term $\chi^{(1)}$ describes the linear refractive index including refraction and absorption and is a result of the dipole response of bound and free electrons to a single photon [1]. The second-order term $\chi^{(2)}$ is a third-rank tensor, nonzero only for non-centrosymmetric materials, describes second-harmonic generation (SHG), sum-and difference frequency generation (SFG, DFG), optical rectification, the Pockels effect and others. The third-order nonlinear optical susceptibility $\chi^{(3)}$ is particularly important because it exists in all materials regardless of the crystal symmetry and gives rise to a rich variety of nonlinear processes, represented by THG [1,97], FWM [78,98], SPM [61,99], and XPM [100,101]. These form the basis of all-optical processing devices, such as wavelength conversion, optical comb generation, quantum entanglement, and more.

Equation (2) gives a simple description of the relevant third-order nonlinear optical effects corresponding to $\widetilde{P}^{(3)}(t) = \varepsilon_0\chi^{(3)}\cdot\widetilde{E}^3(t)$ [97] as follows:

$$\widetilde{P}^{(3)}(t) = \varepsilon_0 \int_{-\infty}^{\infty} \frac{d\omega_1}{2\pi} \int_{-\infty}^{\infty} \frac{d\omega_2}{2\pi} \int_{-\infty}^{\infty} \frac{d\omega_3}{2\pi} \chi^{(3)}(\omega_\sigma; \omega_1, \omega_2, \omega_3) \times E(\omega_1)E(\omega_2)E(\omega_3)e^{-i\omega_\sigma t} \quad (2)$$

where $\omega_\sigma = \omega_1 + \omega_2 + \omega_3$, with ω_1, ω_2, and ω_3 denoting the angular frequencies. Different $\chi^{(3)}$ effects can be described with different wave frequency combinations, such as THG ($\chi^{(3)}(\omega_\sigma = 3\omega_1; \omega_1, \omega_1, \omega_1)$), non-degenerate FWM ($\chi^{(3)}(\omega_\sigma = \omega_1 + \omega_2 - \omega_3; \omega_1, \omega_2, -\omega_3)$) and degenerate FWM ($\chi^{(3)}(\omega_\sigma = 2\omega_1 - \omega_2; \omega_1, \omega_1, -\omega_2)$).

A key component of $\chi^{(3)}$ is given by $n_2 = 3 \cdot \mathrm{Re}\left[\frac{\chi^{(3)}}{4cn_0^2\varepsilon_0}\right]$, which reflects the intensity-dependent refractive index change, known as the Kerr effect and the complex refractive index n can be expressed as [1,97]:

$$n = n_0 + n_2 I - i\frac{\lambda}{4\pi}(\alpha_0 + \alpha_2 I) \quad (3)$$

where n_2 represents the Kerr coefficient or Kerr nonlinearity, I is the light intensity, λ is the wavelength, α_2 is the nonlinear absorption induced by the third-order susceptibility $\chi^{(3)}$, and n_0, α_0 are the linear refractive index and absorption, respectively.

In this paper, we focus on $\chi^{(3)}$ of 2D materials for key nonlinear processes that form the basis for ultra-high speed all-optical signal generation and processing, with response times on the order of femtoseconds [102,103]. These include SPM and XPM, governed largely by n_2 via the Re ($\chi^{(3)}$), as well as FWM and THG that are mainly governed by the magnitude of $|\chi^{(3)}|$, although the latter are also sensitive to the complex value of $\chi^{(3)}$ via phase-matching effects. The n_2 component of $\chi^{(3)}$ accounts for two-photon absorption (TPA) via the Im ($\chi^{(3)}$) and can also result in saturable absorption (SA). Both are intrinsic functions of the material's bandgap, but can also be influenced by free carrier effects. At photon energies well below the bandgap, all $\chi^{(3)}$ components will become degenerate, but near, or above, the bandgap, they will in general be quite different. Finally, since nonlinear absorption is always present, it will affect the efficiency of all third-order nonlinear optical processes, not just n_2, even though it does not arise directly from other $\chi^{(3)}$ components such as THG and FWM, for example. Further, these processes will generally scale differently with pump power to n_2, and so the conventional nonlinear FOM may not be a useful benchmark.

3.2. Characterization Methods

3.2.1. Z-Scan Technique

Measuring the Kerr coefficient of a material is needed in order to design and fabricate nonlinear optical devices. The Z-scan method, introduced in the 1990s [104] is an elegant method to measure the third-order optical Kerr nonlinearity of a material. This technique involves open-aperture (OA) and closed-aperture (CA) measurements, which can be used to measure the third-order nonlinear absorption and nonlinear refraction, respectively. CA Z-scan method is widely used to measure the nonlinear refractive index (Kerr coefficient) of an optical material. The valley–peak and peak–valley transmission curves are the typical results of the CA measurement, as shown in Figure 2a. When the nonlinear material has a positive nonlinear refractive index ($n_2 > 0$), self-focusing will occur which results in the valley–peak transmission curve. The peak–valley CA curve arises from de-focusing and occurs with a negative nonlinear refractive index ($n_2 < 0$).

Figure 2b shows a typical Z-scan setup [62]. To measure the ultrafast nonlinear response, a femtosecond pulsed laser is used to excite the samples. A half-wave plate combined with a linear polarizer can be employed to control the power of the incident light. The beam is focused onto the sample with a lens or an objective. During the measurements, samples are oriented perpendicular to the beam axis and translated along the Z axis with a linear motorized stage. For the measurements of small micrometer sized samples, a high-definition charge-coupled-device imaging system can be employed to align the light beam to the target area. Two PDs are employed to detect the transmitted light power for the signal and reference arms.

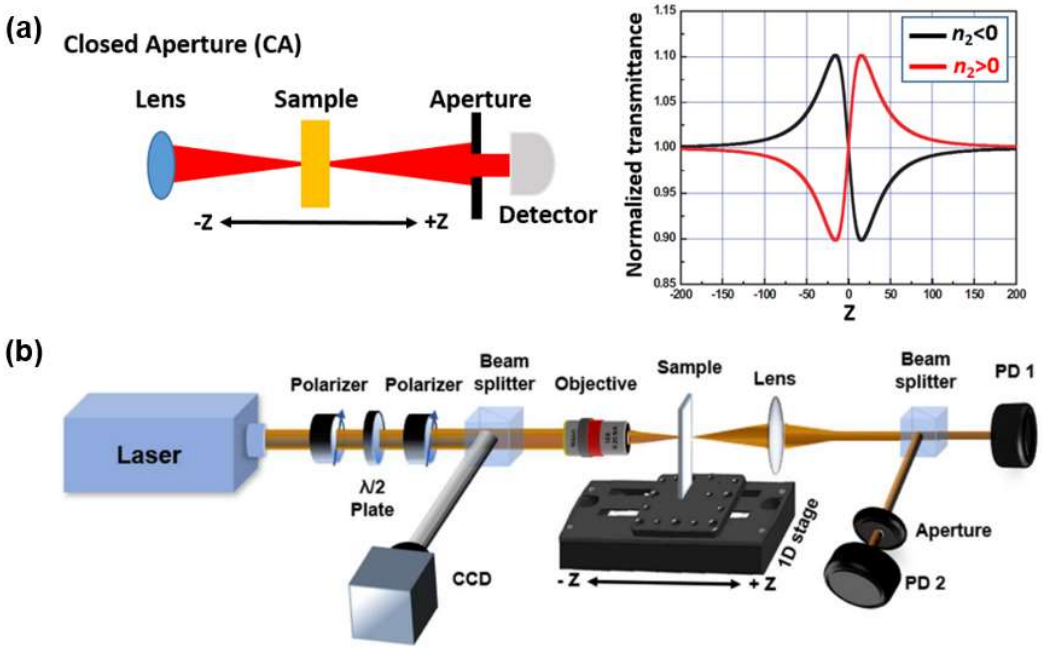

Figure 2. (**a**) Schemes showing the principle of closed-aperture (CA) Z-scan. (**b**) A typical Z-scan setup: PD: power detector, CCD: charge-coupled-device [62].

For the CA Z-scan method, the normalized transmittance can be written as [62,104]:

$$T\left(z,\ \Delta\Phi_0\right) \simeq 1 + \frac{4\Delta\Phi_0 x}{(x^2+9)(x^2+1)} \tag{4}$$

where $x = z/z_0$, $z_0 = k\omega_0^2/2$ with ω_0 the beam waist radius and k the wave vector. $\Delta\Phi_0$ represents the on-axis phase shift at the focus, is defined as [62,104]:

$$\Delta\Phi_0 = kn_2 I_0 L_{eff} \tag{5}$$

In Equation (5), $L_{eff} = \left(1 - e^{-\alpha L}\right)/\alpha$, with L denoting the sample length and α_0 the linear absorption coefficient, k is the wave vector which is defined by $k = 2\pi/\lambda$, and I_0 is the laser irradiance intensity with in the sample [104]. Based on the measured Z-scan curves, one can derive the Kerr coefficient n_2 with the fitting equations.

Graphene is the first 2D material to have been discovered, and its optical nonlinearities have been widely studied using Z-scan measurements and other methods. Figure 3a shows the CA Z-scan signal of a graphene film with an excitation laser wavelength at 1550 nm [105]. A peak–valley configuration can be observed, indicating a negative Kerr nonlinearity. The measured Kerr coefficient n_2 of graphene is as large as 10^{-11} m^2/W which is about six orders of magnitude larger than bulk Si, demonstrating the strong potential of 2D materials for nonlinear optical devices. A laser peak intensity-dependent n_2 has also been observed (Figure 3b), providing a potential method for modulating its nonlinear properties. Figure 3c,d show the CA curves of $CH_3NH_3PbI_3$ perovskite [106] and $Ti_3C_2T_x$ MXene films [57] measured at a wavelength of 1550 nm, where a positive and negative Kerr nonlinearity were observed, respectively. The different response of these two materials forms the basis of their applications in different functional devices. For example, a negative Kerr nonlinearity can be used to self-compress ultrashort pulses in the presence of positive group-velocity dispersion while the materials with positive nonlinearity are promising for achieving a net parametric modulational instability gain under abnormal dispersion conditions.

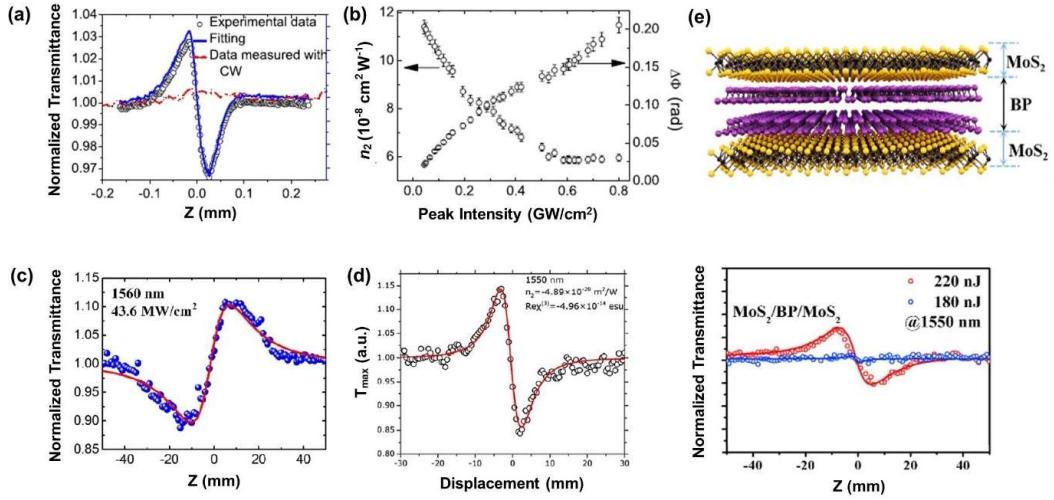

Figure 3. (**a**) CA Z-scan result of graphene under an excitation laser wavelength at 1550 nm. (**b**) Measured n_2 of graphene as a function of laser intensity [105]. (**c**) CA Z-scan result of $CH_3NH_3PbI_3$ under an excitation laser wavelength at 1560 nm [106]. (**d**) CA Z-scan result of MXene films under an excitation laser wavelength at 1550 nm [57]. (**e**) CA Z-scan result of $MoS_2/BP/MoS_2$ heterostructure at different laser intensities. The excitation laser wavelength is 1550 nm [107].

2D van der Waals (vdW) heterostructures offer many new features and possibilities beyond what a single material can provide, and there has been significant activity in this field [107–109]. Recently, the optical nonlinear response of 2D heterostructures has also been investigated via the Z-scan method. Figure 3e plots the CA curve of a $MoS_2/BP/MoS_2$ heterostructure at different laser intensities [107]. A negative Kerr nonlinearity at the telecommunications wavelength of 1550 nm can be observed. The strong Kerr nonlinearity of graphene/Bi_2Te_3 at the same wavelength was also demonstrated recently [110]. By fitting the experimental data, a large n_2 of $\sim 2 \times 10^{-12}$ m^2/W was obtained, which is highly attractive for all-optical modulators and switches.

One of the unique features of GO is its tunable optical and electrical properties through laser reduction, which is particularly attractive for nonlinear optical applications. To investigate laser tunable optical nonlinearities, an in situ third-order Kerr nonlinearity measurement for GO films has been conducted with the Z-scan method [60]. Figure 4a–d show the CA signal of GO films at different laser intensities. At low intensity, GO exhibits a positive Kerr nonlinearity with a valley–peak CA configuration. With increasing the laser intensity, GO reduction occurs and the positive nonlinearity finally transitions into a negative nonlinearity at an intensity of 4.63 GW/cm^2, at which point GO completely reduces to graphene. In addition to the ability to laser tune optical nonlinearities in GO, the measured Kerr coefficient n_2 of GO is as large as 4.5×10^{-14} m^2/W at 1550 nm, which is four orders of magnitude higher than single crystalline silicon. These properties render GO a promising candidate for nonlinear applications in the telecommunications band.

3.2.2. THG Measurement

In addition to the Z-scan method, another technique that can be used to directly characterize the third-order optical nonlinearity of a material is THG measurement. As introduced in Section 3.1, THG is a fundamental third-order optical nonlinear process in which three photons at the same frequency (ω_1) excite the nonlinear media to generate new signal ($\omega = 3\omega_1$). Measuring the THG of a material provides a direct method to characterize its third-order optical nonlinearity. Figure 5 shows a typical setup for THG measurements [111] where a fundamental (ω, red) pulse is incident normally on the sample. The third harmonic (3ω, green) is detected in the reflected direction by a CCD camera, a spectrometer, or a photodiode connected to a lock-in amplifier.

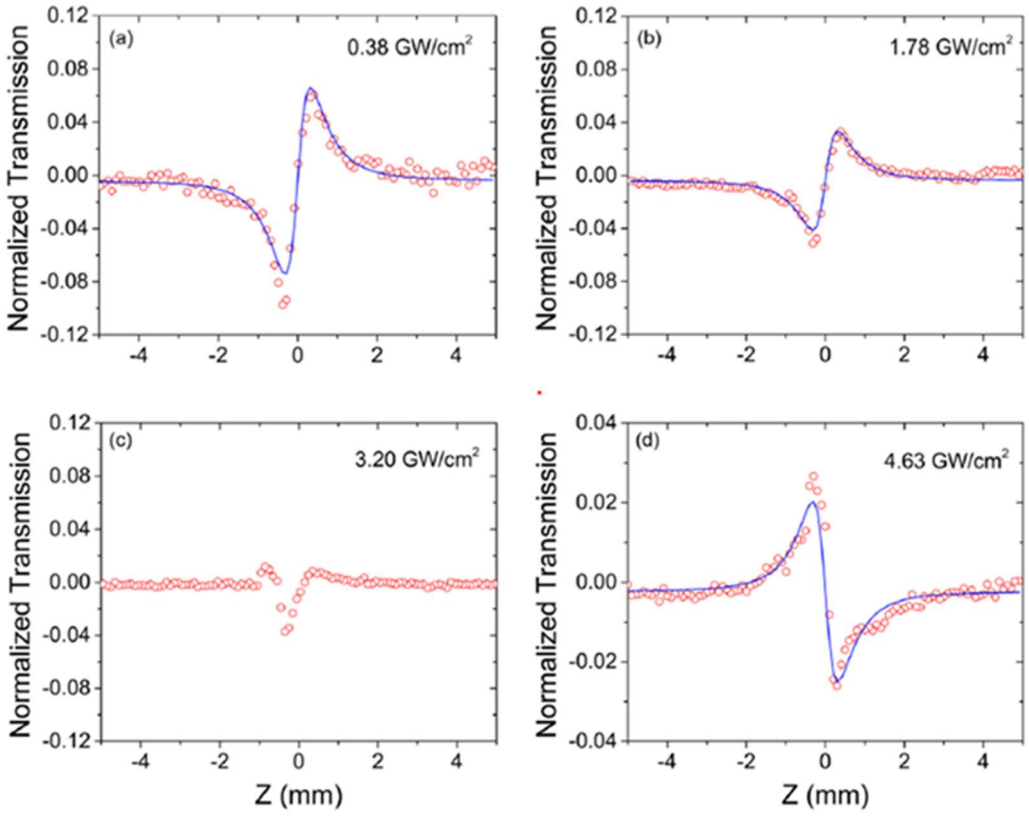

Figure 4. The CA Z-scan results of GO films under different irradiances: (**a**) 0.38 GW/cm^2; (**b**) 1.78 GW/cm^2; (**c**) 3.20 GW/cm^2; (**d**) 4.68 GW/cm^2 [60].

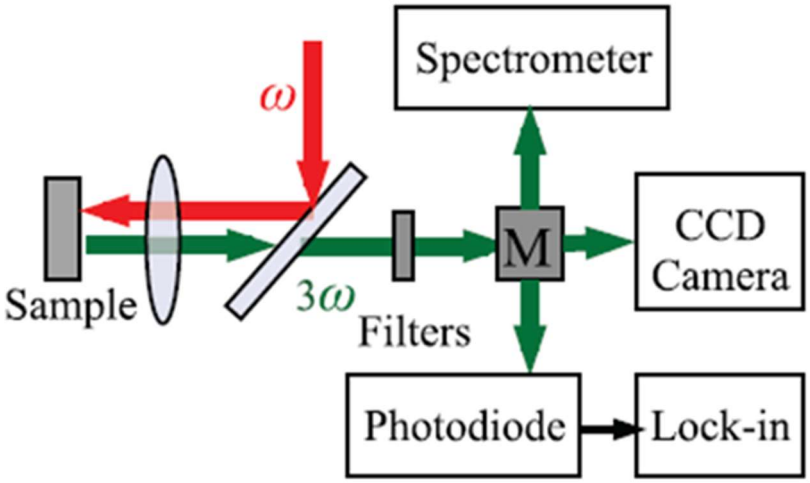

Figure 5. The scheme of a typical THG setup: CCD, charge-coupled-device [111].

To quantitatively analyze the THG effect, an equation for the THG intensity ($I_{3\omega}$), can be introduced [112]:

$$I_{3\omega}(t) = \frac{9\omega^2}{16|\widetilde{n}_{3\omega}||\widetilde{n}_{\omega}|^3\epsilon_0^2c^4} I_{\omega}^3 \left|\chi^{(3)}\right|^2 \left(\frac{e^{-2\alpha t} - 2\cos(\Delta k t)e^{-\alpha t} + 1}{\alpha^2 + \Delta k^2}\right) e^{-2\alpha t} \quad (6)$$

where $\widetilde{n}_{\omega}$ and $\widetilde{n}_{3\omega}$ are the complex refractive indexes at the fundamental and harmonic wavelengths, respectively, α is the absorption coefficient at the THG wavelength, Δk is the phase mismatch between the fundamental and harmonic waves, and $\chi^{(3)}$ is the third-

order susceptibility of the sample. By fitting the THG data with Equation (6), an effective third-order susceptibility $\chi^{(3)}$ value can be obtained.

Strong THG in graphene was demonstrated by Kumar et al. [111]. Figure 6a-i show the THG of monolayer graphene as a function of incident laser powers. The incident laser was 1720.4 nm. By fitting the experimental data, a large $\chi^{(3)}$ of $\sim 0.4 \times 10^{-16}$ m^2/V^2 was obtained. In addition, a thickness-dependent THG signal can be observed (Figure 6a-ii, while $\chi^{(3)}$ remains constant with increasing graphene layer number. Recently, Jiang et al. [113] investigated the gate-tunable THG of graphene. Figure 6b-ii show the THG signal as a function of chemical potential generated at different wavelengths. When tuning the doping level of graphene, an enhanced THG and $\chi^{(3)}$ were observed.

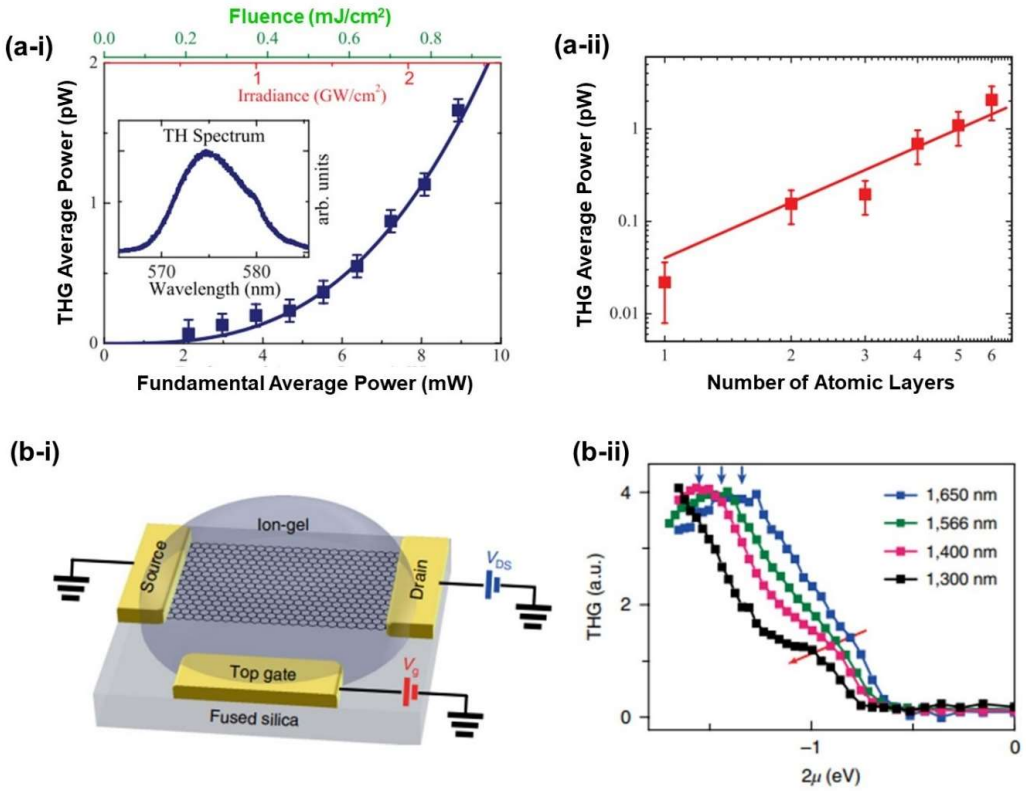

Figure 6. (**a**) THG in graphene: [111] (**a-i**) The average power of the THG signals as a function of the average power of the incident laser. Inset is the THG spectrum. (**a-ii**) The average power of the THG signals as a function of the number of atomic layers for an average fundamental power of 1 mW. (**b**) Gate-tunable THG in graphene: [113] (**b-i**) Schematic of an ion-gel-gated graphene monolayer on a fused silica substrate covered by ion-gel and voltage biased by the top gate. (**b-ii**) THG signal as a function of 2 μ generated by different input wavelengths: 1300 nm, 1400 nm, 1566 nm and 1650 nm.

THG in other 2D materials, such as TMDCs and BP, have also been investigated recently. Rosa et al. [114] characterized THG in mechanically exfoliated WSe_2 flakes at an excitation wavelength of 1560 nm. By measuring the THG for different numbers of layers, a clear thickness-dependent behaviour was observed, as shown in Figure 7a-i,a-iii. The $\chi^{3)}$ of WSe_2 was measured to be in the order of 10^{-19} m^2/V^2, which is comparable to other TMD [115] and BP [116]. Youngblood et al. [116] reported THG in BP by using an ultrafast near-IR laser obtaining a $\chi^{(3)}$ of $\sim 1.4 \times 10^{-19}$ m^2/V^2. In addition, an anisotropic THG was demonstrated, as shown in Figure 7b-iii. Nonlinear optical properties of few-layer GaTe were also studied by characterizing the THG at a pump wavelength of 1560 nm [117]. The THG intensity was found to be sensitive to the number of GaTe layers (Figure 7c-iii). They obtained a large $\chi^{(3)}$ of $\sim 2 \times 10^{-16}$ m^2/V^2

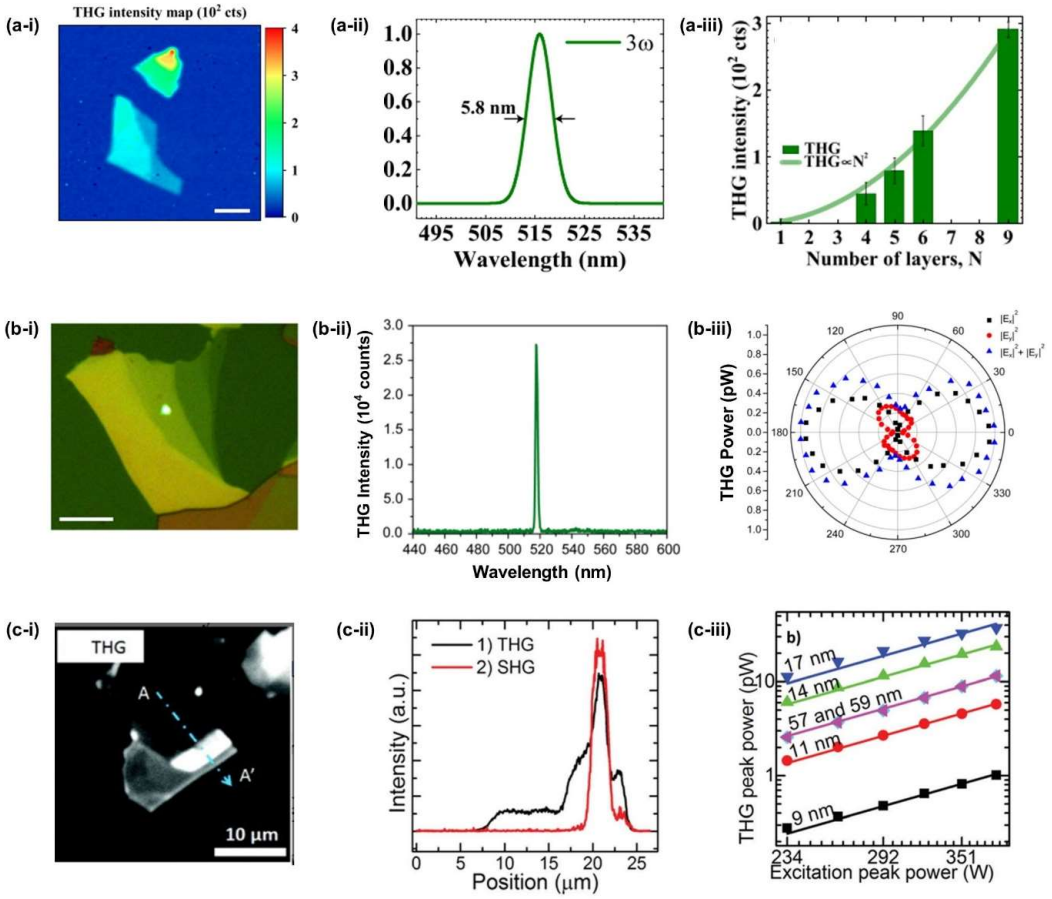

Figure 7. (**a**) THG in WSe_2: [114] (**a-i**) Spatial THG intensity mapping across the WSe_2 sample. (**a-ii**) THG spectrum of WSe_2. (**a-iii**) THG intensities as a function of sample layers. (**b**) THG in BP: [116] (**b-i**) THG emission (bright spot) from the BP flake. (**b-ii**) Measured spectrum of THG emission with a peak wavelength at 519 nm. (**b-iii**) Anisotropic THG in BP. (**c**) THG in GaTe: [117] (**c-i**) THG images of the few-layer GaTe flake. (**c-ii**) Measured spectra of THG emission. (**c-iii**) THG signals of samples with different thicknesses.

3.2.3. Hybrid Device Characterization

Z-scan and THG measurements are usually employed to characterize the material property directly. While on the one hand, the properties of a material form the basis for applications to electronic and optical devices, the reverse is true—device performance can also provide key information about the material properties. A typical example is field effect transistors (FETs) which have been one of the main techniques to evaluate the electrical properties of 2D materials. Optical structures and waveguides can also be exploited to characterize the material optical properties. By integrating 2D materials with photonic cavities and optical waveguides, the third-order optical nonlinearity of atomically thin 2D material has been characterized by measuring the nonlinear optical responses of the hybrid devices, such as FWM [78], SPM [99], and supercontinuum generation [118]. This method also enables the investigation of the layer-dependence of the nonlinear properties, which is challenging for conventional Z-scan methods due to the weak response of ultrathin 2D films.

For the hybrid device characterization, the data analysis is performed in the following steps. First, by fitting the measured FWM or SPM spectra of corresponding hybrid devices, one can obtain the nonlinear parameters (γ) for the bare and hybrid waveguides. Then,

based on the fit γ of the hybrid waveguides, the Kerr coefficient (n_2) of the coated 2D films can be extracted using [119–121]:

$$\gamma = \frac{2\pi}{\lambda} \frac{\iint_D {n_0}^2(x,\ y) n_2(x,\ y) {S_z}^2 dxdy}{\left[\iint_D n_0(x,\ y) S_z dxdy\right]^2} \tag{7}$$

where λ is the central wavelength, D is the integral of the optical fields over the material regions, S_z is the time-averaged Poynting vector calculated using mode solving software, n_0 (x, y) and n_2 (x, y) are the refractive index profiles calculated over the waveguide cross section and the Kerr coefficient of the different material regions, respectively.

FWM is a fundamental third-order nonlinear optical process that has been widely used for all optical signal generation and processing, including wavelength conversion [98,122], optical frequency comb generation [123,124], optical sampling [125,126], quantum entanglement [29,30], and many other processes. The conversion efficiency (CE) of FWM is mainly determined by the third-order Kerr nonlinearity of the material that makes of the device. Therefore, it is useful to obtain the Kerr coefficient of a material by measuring its FWM CE.

Gu et al. [118] fabricated a silicon nanocavity covered with graphene (Figure 8a-i) and measured the FWM CE with different pump and signal detuning wavelengths around 1550 nm, as shown in Figure 8a-ii,a-iii. From the CE data, a n_2 of $\sim 4.8 \times 10^{-17}$ m^2/W was obtained for a graphene integrated with a silicon cavity. The layer-dependence of the Kerr nonlinearity of GO films has been investigated by measuring the FWM performance of GO hybrid devices based on doped-silica and SiN optical waveguides and microring resonators (MRRs) [78,127–129]. Figure 8b-i show a fabricated doped-silica MRR covered with patterned GO films [78]. By fitting the CE to theory for a device with different GO thicknesses, the layer thickness dependence of n_2 of GO at 1550 nm was characterized, as shown in Figure 8b-iii. Recently, electrically tuneable optical nonlinearities of graphene at 1550 nm were also demonstrated by measuring FWM in graphene-SiN waveguides at different gate voltages, as shown in Figure 8c [130].

SPM is another third-order nonlinear optical process that can be used to characterize the optical nonlinearity of 2D materials. Feng et al. [131] studied the Kerr nonlinearities of graphene/Si hybrid waveguides with enhanced SPM (Figure 9a). The n_2 of the Graphene on Si hybrid waveguides was measured to be $\sim 2 \times 10^{-17}$ m^2/W, which is three times larger than that of the Si waveguide. Even though the intrinsic n_2 of graphene is orders of magnitude larger than bulk silicon, the monolayer thickness of the graphene film results in a very low optical mode overlap, which yields only a factor of three improvement in the effective nonlinearity of the waveguide. For GO, on the other hand, comparatively larger film thicknesses are achievable which result in an overall much higher waveguide nonlinearity. Optical nonlinearities of GO films have also been investigated by SPM experiments. Zhang et al. [99] demonstrated the enhanced optical nonlinearity of silicon nanowires integrated with 2D GO Films (Figure 9b-i). Figure 9b-ii show the experimental SPM spectra of the devices with different numbers of GO layers, where increased spectral broadening can be observed in GO coated silicon nanowires. The layer-dependent Kerr n_2 coefficient of GO was also characterized by fitting the spectra to theory, as shown in Figure 9b-iii. In addition to graphene and GO, the optical Kerr nonlinearity of MoS_2 monolayer films was also characterized by analysing the SPM of MoS_2-silicon waveguides [132]. The experiments demonstrated a large Kerr coefficient n_2 of $\sim 1.1 \times 10^{-16}$ m^2/W for a monolayer of MoS_2 in the telecommunications band.

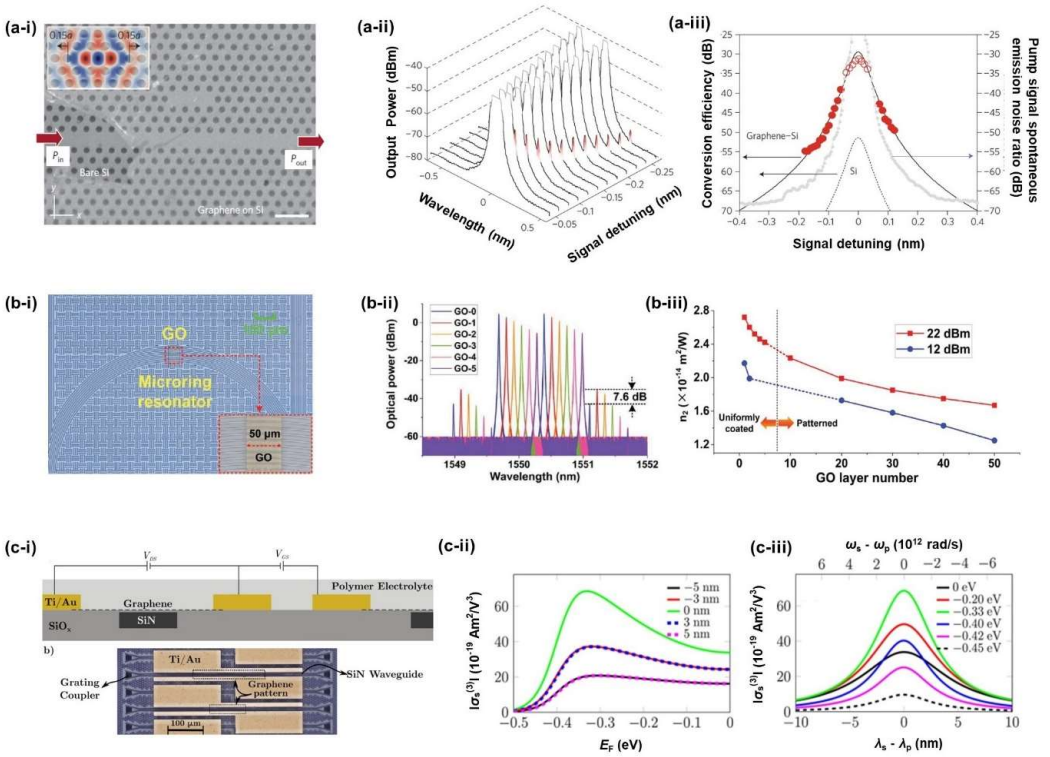

Figure 8. (**a**) FWM in graphene-clad silicon nanocavities: [118] (**a-i**) Scanning electron micrograph (SEM) of the photonic crystal cavity partially covered by graphene monolayer. (**a-ii**) Measured transmission spectrum of the cavity device with pump laser fixed on cavity resonance, and signal laser detuning scanned from 20.04 to 20.27 nm. (**a-iii**) Measured and simulated conversion efficiencies of the cavity. Solid and dashed black lines are modelled conversion efficiencies for the graphene–silicon and monolithic silicon cavities, respectively. (**b**) Layer-dependent optical nonlinearities in GO-coated integrated MRR: [78] (**b-i**) Microscopic image of an integrated MRR patterned with 50 layers of GO. Inset shows zoom-in view of the patterned GO film. (**b-ii**) Optical spectra of FWM at a pump power of 22 dBm for the MRRs with 1−5 layers coated GO. (**b-iii**) n_2 of GO versus layer number at fixed pump powers of 12 and 22 dBm. (**c**) Electrically tunable optical nonlinearities in graphene-covered SiN Waveguides: [130] (**c-i**) Sketch of the gating scheme (up) and optical microscope image (down) of the device. Calculated values of third-order conductivity as a function of Fermi energy for different wavelength detunings (**c-ii**) and as a function of detuning for a range of Fermi energies (**c-iii**).

3.3. Comparison of Measured Results

By using different characterization techniques discussed above, Kerr coefficient n_2 or THG $\chi^{(3)}$ value of graphene, GO, TMDCs, BP, and different heterostructures at telecommunication wavelengths have been obtained. In Table 1, we compare these parameters characterizing the third-order optical nonlinearity. It can be seen that monolayer graphene exhibits the largest n_2 value (up to 10^{-11} m^2/W). The n_2 value of GO films is on the magnitude of 10^{14} m^2/W, which is relatively smaller than graphene, but still more than three orders of magnitudes larger than that of bulk silicon. For MoS_2, MXene film, and 2D heterostructures, the measured n_2 varies from 10^{-16} to 10^{-22} m^2/W. In terms of $\chi^{(3)}$ susceptivity obtained by using THG measurements, the value ranges from 10^{-19} to 10^{-15} m^2/V^2 for graphene, TMDCs, and BP.

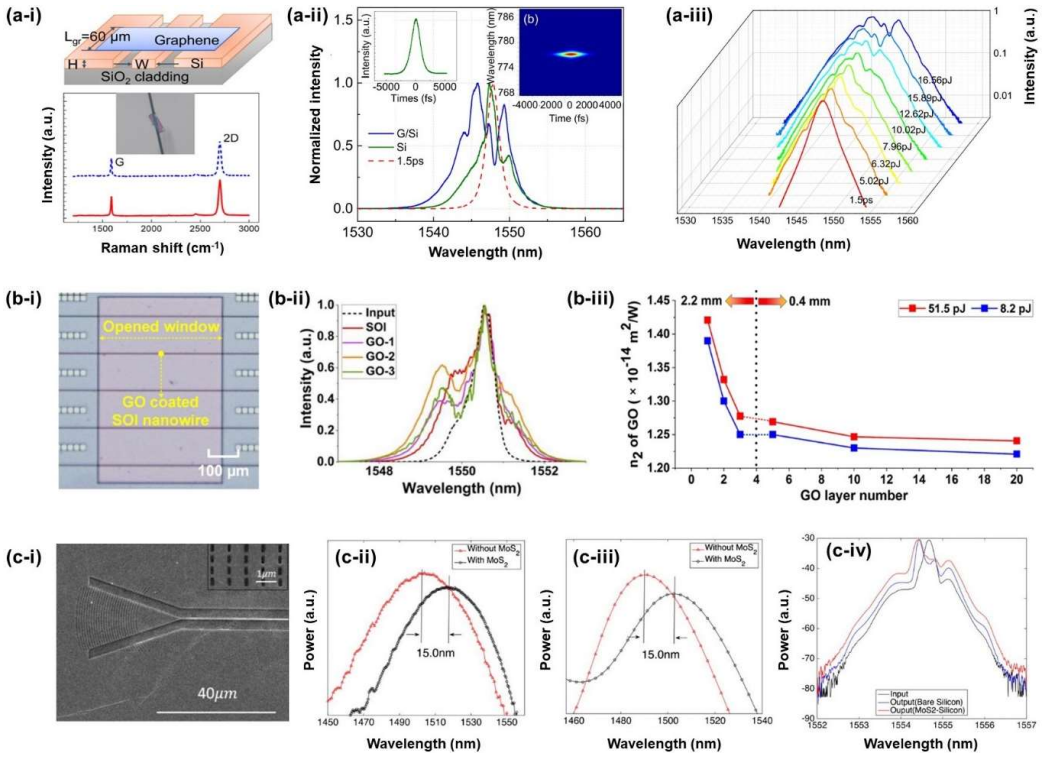

Figure 9. (**a**) SPM experiments in graphene–silicon hybrid waveguides: [131] (**a-i**) Schematic diagram and Raman spectra of the device. (**a-ii**) Measured transmission spectra of comparison between the Si (green solid curve) and G/Si hybrid (blue solid curve) waveguides under the same input energy with 1.5 ps input pulse (spectrum denoted by the red dashed curve). (**a-iii**) Output SPM spectra of the hybrid waveguide under various coupled energies. (**b**) SPM experiments in GO-silicon waveguide: [99] (**b-i**) Microscopic image of a GO-coated silicon nanowire. (**b-ii**) Optical spectra of SPM at a coupled pulse energy of ∼51.5 pJ with 1−3 layers coated GO. (**b-iii**) n_2 of GO vs. layer number at fixed coupled pulse energies of 8.2 and 51.5 pJ. (**c**) SPM experiments in MoS_2-coated silicon waveguides: [132] (**c-i**) scanning electron microscope image of the device, with MoS_2 covering both the grating couplers and waveguide regions. (**c-ii**) Measured transmission spectra of the devices with and without MoS_2. (**c-iii**) Simulation result for the redshift of the grating to estimate the refractive index of MoS_2. (**c-iv**) SPM spectra of MoS_2–silicon waveguide and bare silicon waveguide.

One should note that the measured n_2 values can often vary even for the same material with the use of different measurement techniques, mainly due to the difference in sample preparation and different laser sources used in the measurements. Usually, 2D films fabricated by chemical vapor deposition possess higher numbers of defects compared to mechanically exfoliated single crystal monolayers [37,38], and this can often be reflected in variations in the measured values of n_2. As for the influence of irradiation lasers, the pulse duration is a key factor. In Z-scan and THG measured, a femtosecond laser is widely employed while a picosecond laser or continuous wavelength (CW) laser are used in the characterization of hybrid devices. A longer laser duration, particularly for the CW laser, may induce thermal optical nonlinearity of the materials, resulting in the deviation of the measured n_2 values.

Table 1. Comparison of third-order optical nonlinear parameters of different 2D materials. FWM: four-wave mixing; SPM: self-phase modulation; WG: waveguide; MRR: microring resonator; THG: third-harmonic generation.

Material	Wavelength [(a)]	Thickness	Nonlinear Parameter	Method	Ref.
Graphene	1550 nm	~1 layer	$n_2 = \sim 10^{-11}$ m^2/W	Z-scan	[105]
Graphene	1550 nm	~5–7 layers	$n_2 = \sim -8 \times 10^{-14}$ m^2/W	Z-scan	[58]
GO	1560 nm	~1 um	$n_2 = \sim 4.5 \times 10^{-14}$ m^2/W	Z-scan	[60]
GeP	1550 nm	~15–40 nm	$n_2 = \sim 3.3 \times 10^{-19}$ m^2/W	Z-scan	[133]
$CH_3NH_3PbI_3$	1560 nm	~180 nm	$n_2 = \sim 1.6 \times 10^{-12}$ m^2/W	Z-scan	[106]
MXene	1550 nm	~220 um	$n_2 = \sim -4.89 \times 10^{-20}$ m^2/W	Z-scan	[57]
BiOBr	1550 nm	~140 nm	$n_2 = \sim 3.82 \times 10^{-14}$ m^2/W	Z-scan	[61]
MOF	1550 nm	~4.2 nm	$n_2 = \sim -8.9 \times 10^{-20}$ m^2/W	Z-scan	[134]
MoS_2/BP/MoS_2	1550 nm	~17–20 nm	$n_2 = \sim 3.04 \times 10^{-22}$ m^2/W	Z-scan	[107]
Graphene/Bi_2Te_3	1550 nm	~8.5 nm	$n_2 = \sim 2 \times 10^{-12}$ m^2/W	Z-scan	[110]
Graphene	1550 nm	~1 layer	$n_2 = \sim 10^{-13}$ m^2/W	SPM in WG	[135]
GO	1550 nm	~4 nm	$n_2 = \sim 1.5 \times 10^{-14}$ m^2/W	FWM in WG	[127]
GO	1550 nm	~2–100 nm	$n_2 = \sim (1.2\text{-}2.7) \times 10^{-14}$ m^2/W	FWM in MRR	[78]
GO	1550 nm	~2–20 nm	$n_2 = \sim (1.3\text{-}1.4) \times 10^{-14}$ m^2/W	FWM in WG	[128]
GO	1550 nm	~2–40 nm	$n_2 = \sim (1.2\text{-}1.4) \times 10^{-14}$ m^2/W	SPM in WG	[99]
MoS_2	1550 nm	~1 layer	$n_2 = \sim 1.1 \times 10^{-16}$ m^2/W	SPM in WG	[132]
Graphene	1560 nm	~1 layer	$\chi^{(3)} = \sim 4 \times 10^{-15}$ m^2/V^2	THG	[136]
Graphene	1560 nm	~1 layer	$\chi^{(3)} = \sim 1.5 \times 10^{-19}$ m^2/V^2	THG	[137]
MoS_2	1560 nm	~1 layer	$\chi^{(3)} = \sim 2.4 \times 10^{-19}$ m^2/V^2	THG	[137]
$MoSe_2$	1560 nm	~1 layer	$\chi^{(3)} = \sim 2.2 \times 10^{-19}$ m^2/V^2	THG	[138]
WS_2	1560 nm	~1 layer	$\chi^{(3)} = \sim 2.4 \times 10^{-19}$ m^2/V^2	THG	[138]
WSe_2	1560 nm	~1 layer	$\chi^{(3)} = \sim 1.2 \times 10^{-19}$ m^2/V^2	THG	[114]
$SnSe_2$	1560 nm	multilayer	$\chi^{(3)} = \sim 4.1 \times 10^{-19}$ m^2/V^2	THG	[139]
ReS_2	1515 nm	~1 layer	$\chi^{(3)} = \sim 5.3 \times 10^{-18}$ m^2/V^2	THG	[140]
BP	1560 nm	multilayer	$\chi^{(3)} = \sim 1.6 \times 10^{-19}$ m^2/V^2	THG	[141]

[(a)] Here, is the excitation laser wavelength.

4. Outlook and Prospects

The past decade has witnessed tremendous progress of 2D materials in both fundamental property study and related device applications. As for optical applications, the excellent third-order optical nonlinearity of graphene, GO, TMDCs, and many other novel 2D materials have been investigated using various techniques, and these form the basis of their applications in high-performance nonlinear photonic devices for next-generation optical communications systems.

Despite these remarkable achievements, challenges still exist for engineering the nonlinear optical properties of 2D materials. First, accurate and efficient characterization of the linear and nonlinear optical properties remains challenging. Although the Z-scan method has been highly successful, the very weak Z-scan signals of ultra-thin films limit its applications in mono- or few layer 2D materials, especially for the layer-dependent measurements. In contrast, integrating 2D films with optical waveguides provides a powerful method to obtain accurate nonlinear parameters of atomic-thin 2D materials by analyzing the nonlinear optical performance of the hybrid device. However, the complicated device

fabrication process and resulting relatively low efficiency make this method unsuitable for rapid material characterization which is required for future industrial applications. Second, 2D materials are a large family which include thousands of different materials. For applications of the third-order optical nonlinearity in the telecommunications band, only a very small fraction of them have been investigated. Many newer materials, such as perovskites, MOFs, and graphdiyne, still need more research, which hinders the full exploitation of 2D materials in the fabrication of next-generation nonlinear optical devices. Finally, tuning or engineering the properties of materials is important for both optimizing the device performance and enabling new functionalities, as well as the fundamental study of 2D materials. Nevertheless, current advances in the study of third-order optical nonlinearities of 2D materials focus mainly on their fundamental properties. The relative lack of effective methods of tuning the material properties poses another obstacle for 2D materials to move forward to practical device fabrication. While challenges remain and more work is needed, there is no doubt that 2D materials will underpin key breakthroughs and greatly accelerate the developments of next-generation nonlinear optical devices for many applications, particularly high bandwidth optical communications systems.

5. Conclusions

In conclusion, we review recent progress in the study of the third-order optical nonlinearities of 2D materials in the telecommunications wavelength band. We introduce the representative 2D materials, together with their basic material properties followed by a discussion of the main methods for characterizing the third-order optical nonlinearity, reviewing recent achievements in the field. These advances highlight the significant potential of 2D materials in enabling high-performance nonlinear optical devices for all-optical processing functions in optical communications systems.

Author Contributions: Conceptualization, L.J. and J.W.; writing—original draft preparation, L.J., Y.Z. and Y.Q.; writing—review and editing, J.W. and D.J.M.; supervision, J.W., B.J. and D.J.M.; All authors have read and agreed to the published version of the manuscript.

Funding: This research was funded by the Australian Research Council Discovery Projects Programs (No. DP150102972 and DP190103186), the Swinburne ECR-SUPRA program, the Australian Research Council Industrial Transformation Training Centers scheme (Grant No. IC180100005), and the Beijing Natural Science Foundation (No. Z180007).

Conflicts of Interest: The authors declare no conflict of interest.

References

1. Leuthold, J.; Koos, C.; Freude, W. Nonlinear silicon photonics. *Nat. Photonics* **2010**, *4*, 535–544. [CrossRef]
2. Xia, F.; Sekaric, L.; Vlasov, Y. Ultracompact optical buffers on a silicon chip. *Nat. Photonics* **2007**, *1*, 65–71. [CrossRef]
3. Foster, M.A.; Turner, A.C.; Sharping, J.E.; Schmidt, B.S.; Lipson, M.; Gaeta, A.L. Broad-band optical parametric gain on a silicon photonic chip. *Nature* **2006**, *441*, 960–963. [CrossRef] [PubMed]
4. Razzari, L.; Duchesne, D.; Ferrera, M.; Morandotti, R.; Chu, S.; Little, B.E.; Moss, D.J. CMOS-compatible integrated optical hyper-parametric oscillator. *Nat. Photonics* **2009**, *4*, 41–45. [CrossRef]
5. Ferrera, M.; Razzari, L.; Duchesne, D.; Morandotti, R.; Yang, Z.; Liscidini, M.; Sipe, J.E.; Chu, S.; Little, B.E.; Moss, D.J. Low-power continuous-wave nonlinear optics in doped silica glass integrated waveguide structures. *Nat. Photonics* **2008**, *2*, 737–740. [CrossRef]
6. Gaeta, A.L.; Lipson, M.; Kippenberg, T.J. Photonic-chip-based frequency combs. *Nat. Photonics* **2019**, *13*, 158–169. [CrossRef]
7. Demongodin, P.; Dirani, H.E.; Lhuillier, J.; Crochemore, R.; Kemiche, M.; Wood, T.; Callard, S.; Rojo-Romeo, P.; Sciancalepore, C.; Grillet, C. Ultrafast saturable absorption dynamics in hybrid graphene/Si_3N_4 waveguides. *APL Photonics* **2019**, *4*, 076102. [CrossRef]
8. Aitchison, J.S.; Hutchings, D.C.; Kang, J.U.; Stegeman, G.I.; Villeneuve, A. The nonlinear optical properties of AlGaAs at the half band gap. *IEEE J. Quantum Electron.* **1997**, *33*, 341–348. [CrossRef]
9. Kawashima, H.; Tanaka, Y.; Ikeda, N.; Sugimoto, Y.; Hasama, T.; Ishikawa, H. Optical Bistable Response in AlGaAs-Based Photonic Crystal Microcavities and Related Nonlinearities. *IEEE J. Quantum Electron.* **2008**, *44*, 841–849. [CrossRef]
10. Xie, W.; Chang, L.; Shu, H.; Norman, J.C.; Peters, J.D.; Wang, X.; Bowers, J.E. Ultrahigh-Q AlGaAs-on-insulator microresonators for integrated nonlinear photonics. *Opt. Express* **2020**, *28*, 32894–32906. [CrossRef]

11. Nicoletti, E.; Bulla, D.; Luther-Davies, B.; Gu, M. Generation of lambda/12 nanowires in chalcogenide glasses. *Nano Lett.* **2011**, *11*, 4218–4221. [CrossRef] [PubMed]
12. Eggleton, B.J.; Luther-Davies, B.; Richardson, K. Chalcogenide photonics. *Nat. Photonics* **2011**, *5*, 141–148. [CrossRef]
13. Liang, T.K.; Tsang, H.K. Efficient Raman amplification in silicon-on-insulator waveguides. *Appl. Phys. Lett.* **2004**, *85*, 3343–3345. [CrossRef]
14. Yamashita, D.; Asano, T.; Susumu, N.; Takahashi, Y. Strongly asymmetric wavelength dependence of optical gain in nanocavity-based Raman silicon lasers. *Optica* **2018**, *5*, 1256–1263. [CrossRef]
15. Zhang, Y.; Zhong, K.; Tsang, H.K. Raman Lasing in Multimode Silicon Racetrack Resonators. *Laser Photonics Rev.* **2020**, *15*, 2000336. [CrossRef]
16. Salem, R.; Foster, M.A.; Turner, A.C.; Geraghty, D.F.; Lipson, M. Signal regeneration using low-power four-wave mixing on silicon chip. *Nat. Photonics* **2008**, *2*, 35–38. [CrossRef]
17. Mathlouthi, W.; Rong, H.; Paniccia, M. Characterization of efficient wavelength conversion by four-wave mixing in sub-micron silicon waveguides. *Opt. Express* **2008**, *16*, 16735–16745. [CrossRef]
18. Frigg, A.; Boes, A.; Ren, G.; Nguyen, T.G.; Choi, D.-Y.; Gees, S.; Moss, D.; Mitchell, A. Optical frequency comb generation with low temperature reactive sputtered silicon nitride waveguides. *APL Photonics* **2020**, *5*, 011302. [CrossRef]
19. Li, F.; Vo, T.D.; Husko, C.; Pelusi, M.; Xu, D.-X.; Densmore, A.; Ma, R.; Janz, S.; Eg-gleton, B.J.; Moss, D.J. All-optical XOR logic gate for 40 Gb/s DPSK signals via FWM in a silicon nanowire. *Opt. Express* **2011**, *19*, 20364–20371. [CrossRef]
20. Gao, S.; Wang, X.; Xie, Y.; Hu, P.; Yan, Q. Reconfigurable dual-channel all-optical logic gate in a silicon waveguide using polarization encoding. *Opt. Lett.* **2015**, *40*, 1448–1451. [CrossRef]
21. Soref, R.; De Leonardis, F.; Ying, Z.; Passaro, V.M.N.; Chen, R.T. Silicon-Based Group-IV O-E-O Devices for Gain, Logic, and Wavelength Conversion. *ACS Photonics* **2020**, *7*, 800–811. [CrossRef]
22. Monat, C.; Grillet, C.; Collins, M.; Clark, A.; Schroeder, J.; Xiong, C.; Li, J.; O'Faolain, L.; Krauss, T.F.; Eggleton, B.J. Integrated optical auto-correlator based on third-harmonic generation in a silicon photonic crystal waveguide. *Nat. Commun.* **2014**, *5*, 3246. [CrossRef] [PubMed]
23. Wu, J.; Xu, X.; Nguyen, T.G.; Chu, S.T.; Little, B.E.; Morandotti, R.; Mitchell, A.; Moss, D.J. RF Photonics: An Optical Microcombs' Perspective. *IEEE J. Sel. Top. Quantum Electron.* **2018**, *24*, 1–20. [CrossRef]
24. Xu, X.; Wu, J.; Nguyen, T.G.; Chu, S.T.; Little, B.E.; Morandotti, R.; Mitchell, A.; Moss, D.J. Broadband RF Channelizer Based on an Integrated Optical Frequency Kerr Comb Source. *J. Lightwave Technol.* **2018**, *36*, 4519–4526. [CrossRef]
25. Xu, X.; Tan, M.; Wu, J.; Morandotti, R.; Mitchell, A.; Moss, D.J. Microcomb-Based Photonic RF Signal Processing. *IEEE Photonics Technol. Lett.* **2019**, *31*, 1854–1857. [CrossRef]
26. Corcoran, B.; Corcoran, B.; Tan, M.; Xu, X.; Boes, A.; Wu, J.; Nguyen, T.G.; Chu, S.T. Ultra-dense optical data transmission over standard fibre with a single chip source. *Nat. Commun.* **2020**, *11*, 2568. [CrossRef] [PubMed]
27. Fridman, M.; Farsi, A.; Okawachi, Y.; Gaeta, A.L. Demonstration of temporal cloaking. *Nature* **2012**, *481*, 62–65. [CrossRef]
28. Reimer, C.; Kues, M.; Roztocki, P.; Wetzel, B.; Grazioso, F.; Little, B.E.; Chu, S.T.; Johnston, T.; Bromberg, Y.; Caspani, L.; et al. Generation of multiphoton entangled quantum states by means of integrated frequency combs. *Science* **2016**, *351*, 1176–1180. [CrossRef]
29. Kues, M.; Reimer, C.; Roztocki, P.; Cortés, L.R.; Sciara, S.; Wetzel, B.; Zhang, Y.; Cino, A.; Chu, S.T.; Little, B.E.; et al. On-chip generation of high-dimensional entangled quantum states and their coherent control. *Nature* **2017**, *546*, 622–626. [CrossRef]
30. Caspani, L.; Xiong, C.; Eggleton, B.J.; Bajoni, D.; Liscidini, M.; Galli, M.; Morandotti, R.; Moss, D.J. Integrated sources of photon quantum states based on nonlinear optics. *Light Sci. Appl.* **2017**, *6*, e17100. [CrossRef]
31. Geim, A.K.; Novoselov, K.S. The rise of graphene. *Nat. Mater.* **2007**, *6*, 183–191. [CrossRef]
32. Yang, T.; Lin, H.; Zheng, X.; Loh, K.P.; Jia, B. Tailoring pores in graphene-based materials: From generation to applications. *J. Mater. Chem. A* **2017**, *5*, 16537–16558. [CrossRef]
33. Bolotin, K.I.; Sikes, K.J.; Hone, J.; Stormer, H.L.; Kim, P. Temperature-dependent transport in suspended graphene. *Phys. Rev. Lett.* **2008**, *101*, 096802. [CrossRef]
34. Loh, K.P.; Bao, Q.; Eda, G.; Chhowalla, M. Graphene oxide as a chemically tunable platform for optical applications. *Nat. Chem.* **2010**, *2*, 1015–1024. [CrossRef] [PubMed]
35. Ghofraniha, N.; Conti, C. Graphene oxide photonics. *J. Opt.* **2019**, *21*, 053001. [CrossRef]
36. Luo, Z.; Vora, P.M.; Mele, E.J.; Johnson, A.T.C.; Kikkawa, J.M. Photoluminescence and band gap modulation in graphene oxide. *Appl. Phys. Lett.* **2009**, *94*, 111909. [CrossRef]
37. Tian, H.; Chin, M.L.; Najmaei, S.; Guo, Q.; Xia, F.; Wang, H.; Dubey, M. Optoelectronic devices based on two-dimensional transition metal dichalcogenides. *Nano Res.* **2016**, *9*, 1543–1560. [CrossRef]
38. Tan, T.; Jiang, X.; Wang, C.; Yao, B.; Zhang, H. 2D Material Optoelectronics for Information Functional Device Applications: Status and Challenges. *Adv. Sci.* **2020**, *7*, 2000058. [CrossRef] [PubMed]
39. Liang, Q.; Wang, Q.; Zhang, Q.; Wei, J.; Lim, S.X.; Zhu, R.; Hu, J.; Wei, W.; Lee, C.; Sow, C. High-Performance, Room Temperature, Ultra-Broadband Photodetectors Based on Air-Stable $PdSe_2$. *Adv. Mater.* **2019**, *31*, e1807609. [CrossRef]
40. Pi, L.; Pi, L.; Li, L.; Liu, K.; Zhang, Q.; Li, H.; Zhai, T. Recent Progress on 2D Noble-Transition-Metal Dichalcogenides. *Adv. Funct. Mater.* **2019**, *29*, 1904932. [CrossRef]

41. Zhang, K.; Feng, Y.; Wang, F.; Yang, Z.; Wang, J. Two dimensional hexagonal boron nitride (2D-hBN): Synthesis, properties and applications. *J. Mater. Chem. C* **2017**, *5*, 11992–12022. [CrossRef]
42. Tran, T.T.; Bray, K.; Ford, M.J.; Toth, M.; Aharonovich, I. Quantum emission from hexagonal boron nitride monolayers. *Nat. Nanotechnol.* **2016**, *11*, 37–41. [CrossRef]
43. Caldwell, J.D.; Aharonovich, I.; Cassabois, G.; Edgar, J.H.; Gil, B.; Basov, D.N. Photonics with hexagonal boron nitride. *Nat. Rev. Mater.* **2019**, *4*, 552–567. [CrossRef]
44. Autere, A.; Jussila, H.; Dai, Y.; Wang, Y.; Lipsanen, H.; Sun, Z. Nonlinear Optics with 2D Layered Materials. *Adv. Mater.* **2018**, *30*, 1705963. [CrossRef]
45. Qiao, J.; Kong, X.; Hu, Z.-X.; Yang, F.; Ji, W. High-mobility transport anisotropy and linear dichroism in few-layer black phosphorus. *Nat. Commun.* **2014**, *5*, 4475. [CrossRef]
46. Yuan, H.; Liu, X.; Afshinmanesh, F.; Li, W.; Xu, G.; Sun, J.; Lian, B.; Curto, A.G.; Ye, G.; Hikita, Y.; et al. Polarization-sensitive broadband photodetector using a black phosphorus vertical p–n junction. *Nat. Nanotechnol.* **2015**, *10*, 707–713. [CrossRef]
47. Guo, Q.; Pospischil, A.; Bhuiyan, M.; Jiang, H.; Tian, H.; Farmer, D.; Deng, B.; Li, C.; Han, S.-J.; Wang, H.; et al. Black Phosphorus Mid-Infrared Photodetectors with High Gain. *Nano Lett.* **2016**, *16*, 4648–4655. [CrossRef]
48. Li, L.; Kim, J.; Jin, C.; Ye, G.J.; Qiu, D.Y.; da Jornada, F.H.; Shi, Z.; Chen, L.; Zhang, Z.; Yang, F.; et al. Direct observation of the layer-dependent electronic structure in phosphorene. *Nat. Nanotechnol.* **2017**, *12*, 21–25. [CrossRef] [PubMed]
49. Radisavljevic, B.; Radenovic, A.; Brivio, J.; Giacometti, V.; Kis, A. Single-layer MoS_2 transistors. *Nat. Nanotechnol.* **2011**, *6*, 147–150. [CrossRef] [PubMed]
50. Fang, H.; Chuang, S.; Chang, T.C.; Takei, K.; Takahashi, T.; Javey, A. High performance single layered WSe_2 p-FETs with chemically doped contacts. *Nano Lett.* **2012**, *12*, 3788–3792. [CrossRef] [PubMed]
51. Lee, M.M.; Teuscher, J.; Miyasaka, T.; Murakami, T.N.; Snaith, H.J. Efficient Hybrid Solar Cells Based on Meso-Superstructured Organometal Halide Perovskites. *Science* **2012**, *338*, 643–647. [CrossRef]
52. Xing, J.; Yan, F.; Zhao, Y.; Chen, S.; Yu, H.; Zhang, Q.; Zeng, R.; Demir, H.V.; Sun, X.; Huan, A.; et al. High-Efficiency Light-Emitting Diodes of Organometal Halide Perovskite Amorphous Nanoparticles. *ACS Nano* **2016**, *10*, 6623–6630. [CrossRef] [PubMed]
53. Zhang, J.; Jiang, T.; Zheng, X.; Shen, C.; Cheng, X. Thickness-dependent nonlinear optical properties of $CsPbBr_3$ perovskite nanosheets. *Opt. Lett.* **2017**, *42*, 3371–3374. [CrossRef] [PubMed]
54. Sun, Z.; Hasan, T.; Torrisi, F.; Popa, D.; Privitera, G.; Wang, F.; Bonaccorso, F.; Basko, D.M.; Ferrari, A.C. Graphene Mode-Locked Ultrafast Laser. *ACS Nano* **2010**, *4*, 803–810. [CrossRef]
55. Zhang, J.; Ouyang, H.; Zheng, X.; You, J.; Chen, R.; Zhou, T.; Sui, Y.; Liu, Y.; Cheng, X.; Jiang, T. Ultrafast saturable absorption of MoS_2 nanosheets under different pulse-width excitation conditions. *Opt. Lett.* **2018**, *43*, 243–246. [CrossRef] [PubMed]
56. Wang, S.; Yu, H.; Zhang, H.; Wang, A.; Zhao, M.; Chen, Y.; Mei, L.; Wang, J. Broadband few-layer MoS2 saturable absorbers. *Adv. Mater.* **2014**, *26*, 3538–3544. [CrossRef] [PubMed]
57. Jiang, X.; Liu, S.; Liang, W.; Luo, S.; He, Z.; Ge, Y.; Wang, H.; Cao, R.; Zhang, F.; Wen, Q.; et al. Broadband Nonlinear Photonics in Few-Layer MXene Ti_3C_2Tx (T = F, O, or OH). *Laser Photonics Rev.* **2018**, *12*, 1700229. [CrossRef]
58. Demetriou, G.; Bookey, H.T.; Biancalana, F.; Abraham, E.; Wang, Y.; Ji, W.; Kar, A.K. Nonlinear optical properties of multilayer graphene in the infrared. *Opt. Express* **2016**, *24*, 13033–13043. [CrossRef]
59. Zheng, X.; Jia, B.; Chen, X.; Gu, M. In situ third-order non-linear responses during laser reduction of graphene oxide thin films towards on-chip non-linear photonic devices. *Adv. Mater.* **2014**, *26*, 2699–2703. [CrossRef]
60. Xu, X.; Zheng, X.; He, F.; Wang, Z.; Subbaraman, H.; Wang, Y.; Jia, B.; Chen, R.T. Observation of Third-order Nonlinearities in Graphene Oxide Film at Telecommunication Wavelengths. *Sci. Rep.* **2017**, *7*, 9646. [CrossRef]
61. Jia, L.; Cui, D.; Wu, J.; Feng, H.; Yang, Y.; Yang, T.; Qu, Y.; Du, Y.; Hao, W.; Jia, B.; et al. Highly nonlinear BiOBr nanoflakes for hybrid integrated photonics. *APL Photonics* **2019**, *4*, 090802. [CrossRef]
62. Jia, L.N.; Wu, J.Y.; Yang, T.S.; Jia, B.H.; Moss, D.J. Large Third-Order Optical Kerr Nonlinearity in Nanometer-Thick PdSe2 2D Dichalcogenide Films: Implications for Nonlinear Photonic Devices. *ACS Appl. Nano Mater.* **2020**, *3*, 6876–6883. [CrossRef]
63. Yoshikawa, N.; Tamaya, T.; Tanaka, K. High-harmonic generation in graphene enhanced by elliptically polarized light excitation. *Science* **2017**, *356*, 736–738. [CrossRef] [PubMed]
64. Janisch, C.; Wang, Y.; Ma, D.; Mehta, N.; Elias, A.L.; Perea-Lopez, N.; Terrones, M.; Crespi, V.; Liu, Z. Extraordinary Second Harmonic Generation in tungsten disulfide monolayers. *Sci. Rep.* **2014**, *4*, 5530. [CrossRef] [PubMed]
65. Karvonen, L.; Säynätjoki, A.; Mehravar, S.; Rodriguez, R.; Hartmann, S.; Zahn, D.; Honkanen, S.; Norwood, R.; Peyghambarian, N.; Kieu, K.; et al. Investigation of second-and third-harmonic generation in few-layer gallium selenide by multiphoton microscopy. *Sci. Rep.* **2015**, *5*, 1–8. [CrossRef]
66. Jiang, T.; Kravtsov, V.; Tokman, M.; Belyanin, A.; Raschke, M.B. Ultrafast coherent nonlinear nanooptics and nanoimaging of graphene. *Nat. Nanotechnol.* **2019**, *14*, 838–843. [CrossRef]
67. Foster, M.A.; Salem, R.; Geraghty, D.F.; Turner-Foster, A.C.; Lipson, M.; Gaeta, A.L. Silicon-chip-based ultrafast optical oscilloscope. *Nature* **2008**, *456*, 81–84. [CrossRef] [PubMed]
68. Zhong, H.-S.; Wang, H.; Deng, Y.-H.; Chen, M.-C.; Peng, L.-C.; Luo, Y.-H.; Qin, J.; Wu, D.; Ding, X.; Hu, Y.; et al. Quantum computational advantage using photons. *Science* **2020**, *370*, 1460–1463. [CrossRef] [PubMed]
69. Chen, W.; Zhang, F.; Wang, C.; Jia, M.; Zhao, X.; Liu, Z.; Ge, Y.; Zhang, Y.; Zhang, H. Nonlinear Photonics Using Low-Dimensional Metal-Halide Perovskites: Recent Advances and Future Challenges. *Adv. Mater.* **2021**, *33*, e2004446. [CrossRef]

70. Liu, W.; Liu, M.; Liu, X.; Wang, X.; Deng, H.X.; Lei, M.; Wei, Z.; Wei, Z. Recent Advances of 2D Materials in Nonlinear Photonics and Fiber Lasers. *Adv. Opt. Mater.* **2020**, *8*, 1901631. [CrossRef]
71. Nair, R.R.; Blake, P.; Grigorenko, A.N.; Novoselov, K.S.; Booth, T.J.; Stauber, T.; Peres, N.M.R.; Geim, A.K. Fine Structure Constant Defines Visual Transparency of Graphene. *Science* **2008**, *320*, 1308. [CrossRef]
72. Lui, C.H.; Mak, K.F.; Shan, J.; Heinz, T.F. Ultrafast Photoluminescence from Graphene. *Phys. Rev. Lett.* **2010**, *105*, 127404. [CrossRef]
73. Sun, Z.; Martinez, A.; Wang, F. Optical modulators with 2D layered materials. *Nat. Photonics* **2016**, *10*, 227–238. [CrossRef]
74. Li, F.; Zhao, J.; Liu, L. *Graphene Oxide-Physics and Applications*; Springer: Berlin/Heidelberg, Germany, 2015.
75. Bao, Q.; Zhang, H.; Wang, Y.; Ni, Z.; Yan, Y.; Shen, Z.X.; Loh, K.P.; Tang, D.Y. Atomic-Layer Graphene as a Saturable Absorber for Ultrafast Pulsed Lasers. *Adv. Funct. Mater.* **2009**, *19*, 3077–3083. [CrossRef]
76. Zhu, G.; Zhu, X.; Wang, F.; Xu, S.; Li, Y.; Guo, X.; Balakrishnan, K.; Norwood, R.A.; Peyghambarian, N. Graphene Mode-Locked Fiber Laser at 2.8 μm. *IEEE Photonics Technol. Lett.* **2016**, *28*, 7–10. [CrossRef]
77. Wu, R.; Zhang, Y.; Yan, S.; Bian, F.; Wang, W.; Bai, X.; Lu, X.; Zhao, J. Purely coherent nonlinear optical response in solution dispersions of graphene sheets. *Nano Lett.* **2011**, *11*, 5159–5164. [CrossRef]
78. Wu, J.; Yang, Y.; Qu, Y.; Jia, L.; Zhang, Y.; Xu, X.; Chu, S.T.; Little, B.E.; Morandotti, R.; Jia, B.; et al. 2D Layered Graphene Oxide Films Integrated with Micro-Ring Resonators for Enhanced Nonlinear Optics. *Small* **2020**, *16*, e1906563. [CrossRef] [PubMed]
79. Hendry, E.; Hale, P.J.; Moger, J.; Savchenko, A.K.; Mikhailov, S.A. Coherent nonlinear optical response of graphene. *Phys. Rev. Lett.* **2010**, *105*, 097401. [CrossRef]
80. Splendiani, A.; Sun, L.; Zhang, Y.; Li, T.; Kim, J.; Chim, C.Y.; Galli, G.; Wang, F. Emerging photoluminescence in monolayer MoS_2. *Nano Lett.* **2010**, *10*, 1271–1275. [CrossRef]
81. Mak, K.F.; Xiao, D.; Shan, J. Light–valley interactions in 2D semiconductors. *Nat. Photonics* **2018**, *12*, 451–460. [CrossRef]
82. Xu, N.; Wang, H.; Zhang, H.; Guo, L.; Shang, X.; Jiang, S.; Li, D. Palladium diselenide as a direct absorption saturable absorber for ultrafast mode-locked operations: From all anomalous dispersion to all normal dispersion. *Nanophotonics* **2020**, *9*, 267. [CrossRef]
83. Yang, T.; Abdelwahab, I.; Lin, H.; Bao, Y.; Rong Tan, S.J.; Fraser, S.; Loh, K.P.; Jia, B. Anisotropic Third-Order Nonlinearity in Pristine and Lithium Hydride Intercalated Black Phosphorus. *ACS Photonics* **2018**, *5*, 4969–4977. [CrossRef]
84. Zhao, Y.; Chen, Y.; Zhang, Y.-H.; Liu, S.-F. Recent advance in black phosphorus: Properties and applications. *Mater. Chem. Phys.* **2017**, *189*, 215–229. [CrossRef]
85. Wu, H.-Y.; Yen, Y.; Liu, C.-H. Observation of polarization and thickness dependent third-harmonic generation in multilayer black phosphorus. *Appl. Phys. Lett.* **2016**, *109*, 261902. [CrossRef]
86. Wang, Y.; Huang, G.; Mu, H.; Lin, S.; Chen, J.; Xiao, S.; Bao, Q.; He, J. Ultrafast recovery time and broadband saturable absorption properties of black phosphorus suspension. *Appl. Phys. Lett.* **2015**, *107*, 091905. [CrossRef]
87. Wang, K.; Szydlowska, B.M.; Wang, G.; Zhang, X.; Wang, J.J.; Magan, J.J.; Zhang, L.; Coleman, J.N.; Wang, J.; Blau, W.J. Ultrafast Nonlinear Excitation Dynamics of Black Phosphorus Nanosheets from Visible to Mid-Infrared. *ACS Nano* **2016**, *10*, 6923–6932. [CrossRef]
88. Luo, Z.C.; Liu, M.; Guo, Z.N.; Jiang, X.F.; Luo, A.P.; Zhao, C.J.; Yu, X.F.; Xu, W.C.; Zhang, H. Microfiber-based few-layer black phosphorus saturable absorber for ultra-fast fiber laser. *Opt. Express* **2015**, *23*, 20030–20039. [CrossRef] [PubMed]
89. Wang, J.; Ma, F.; Sun, M. Graphene, hexagonal boron nitride, and their heterostructures: Properties and applications. *RSC Adv.* **2017**, *7*, 16801–16822. [CrossRef]
90. Naguib, M.; Kurtoglu, M.; Presser, V.; Lu, J.; Niu, J.; Heon, M.; Hultman, L.; Gogotsi, Y.; Barsoum, M.W. Two-dimensional nanocrystals produced by exfoliation of Ti_3AlC_2. *Adv. Mater.* **2011**, *23*, 4248–4253. [CrossRef]
91. Dillon, A.D.; Ghidiu, M.J.; Krick, A.L.; Griggs, J.; May, S.J.; Gogotsi, Y.; Barsoum, M.W.; Fafarman, A.T. Highly Conductive Optical Quality Solution-Processed Films of 2D Titanium Carbide. *Adv. Funct. Mater.* **2016**, *26*, 4162–4168. [CrossRef]
92. Stranks, S.D.; Snaith, H.J. Metal-halide perovskites for photovoltaic and light-emitting devices. *Nat. Nanotechnol.* **2015**, *10*, 391–402. [CrossRef]
93. Gu, C.; Zhang, H.; You, P.; Zhang, Q.; Luo, G.; Shen, Q.; Wang, Z.; Hu, J. Giant and Multistage Nonlinear Optical Response in Porphyrin-Based Surface-Supported Metal-Organic Framework Nanofilms. *Nano Lett.* **2019**, *19*, 9095–9101. [CrossRef]
94. Liu, W.; Yin, R.; Xu, X.; Zhang, L.; Shi, W.; Cao, X. Structural Engineering of Low-Dimensional Metal-Organic Frameworks: Synthesis, Properties, and Applications. *Adv. Sci.* **2019**, *6*, 1802373. [CrossRef]
95. Medishetty, R.; Zareba, J.K.; Mayer, D.; Samoc, M.; Fischer, R.A. Nonlinear optical properties, upconversion and lasing in metal-organic frameworks. *Chem. Soc. Rev.* **2017**, *46*, 4976–5004. [CrossRef]
96. Zheng, Y.; Sun, F.Z.; Han, X.; Xu, J.; Bu, X.H. Recent Progress in 2D Metal-Organic Frameworks for Optical Applications. *Adv. Opt. Mater.* **2020**, *8*, 2000110. [CrossRef]
97. Boyd, R.W. *Nonlinear Optics*; Elsevier: Rochester, NY, USA, 2007.
98. Moss, D.J.; Morandotti, R.; Gaeta, A.L.; Lipson, M. New CMOS-compatible platforms based on silicon nitride and Hydex for nonlinear optics. *Nat. Photonics* **2013**, *7*, 597–607. [CrossRef]
99. Zhang, Y.Y.; Wu, J.; Yang, Y.; Qu, Y.; Jia, L.; Moein, T.; Jia, B.; Moss, D.J. Enhanced Kerr Nonlinearity and Nonlinear Figure of Merit in Silicon Nanowires Integrated with 2D Graphene Oxide Films. *ACS Appl. Mater. Interfaces* **2020**, *12*, 33094–33103. [CrossRef] [PubMed]

100. Li, Y.; Kang, Z.; Zhu, K.; Ai, S.; Wang, X.; Davidson, R.R.; Wu, Y.; Morandotti, R.; Little, B.E.; Moss, D.J.; et al. All-optical RF spectrum analyzer with a 5 THz bandwidth based on CMOS-compatible high-index doped silica waveguides. *Opt. Lett.* **2021**, *46*, 1574. [CrossRef] [PubMed]
101. Ferrera, M.; Reimer, C.; Pasquazi, A.; Peccianti, M.; Clerici, M.; Caspani, L.; Chu, S.T.; Little, B.E.; Morandotti, R.; Moss, D.J. CMOS compatible integrated all-optical radio frequency spectrum analyzer. *Opt. Express* **2014**, *22*, 21488–21498. [CrossRef] [PubMed]
102. Corcoran, B.; Monat, C.; Grillet, C.; Moss, D.J.; Eggleton, B.J.; White, T.P.; O'Faolain, L.; Krauss, T.F. Green light emission in silicon through slow-light enhanced third-harmonic generation in photonic-crystal waveguides. *Nat. Photonics* **2009**, *3*, 206–210. [CrossRef]
103. Corcoran, B.; Monat, C.; Pelusi, M.; Grillet, C.; White, T.P.; O'Faolain, L.; Krauss, T.F.; Eggleton, B.J.; Moss, D.J. Optical signal processing on a silicon chip at 640 Gb/s using slow-light. *Opt. Express* **2010**, *18*, 7770–7781. [CrossRef]
104. Mansoor Sheik-Bahae, A.A.S.; Wei, T.-H.; Hagan, D.J.; van Stryland, E.W. Sensitive Measurement of Optical Nonlinearities Using a Single Beam. *IEEE J. Quantum Electron.* **1990**, *26*, 760–769. [CrossRef]
105. Zhang, H.; Virally, S.; Bao, Q.; Kian Ping, L.; Massar, S.; Godbout, N.; Kockaert, P. Z-scan measurement of the nonlinear refractive index of graphene. *Opt. Lett.* **2012**, *37*, 1856–1858. [CrossRef] [PubMed]
106. Yi, J.; Miao, L.; Li, J.; Hu, W.; Zhao, C.; Wen, S. Third-order nonlinear optical response of $CH_3NH_3PbI_3$ perovskite in the mid-infrared regime. *Opt. Mater. Express* **2017**, *7*, 3894–3901. [CrossRef]
107. Xiao, S.; Wang, H.; Qin, Y.; Li, X.; Xin, H.; Wang, G.; Hu, L.; Wang, Y.; Li, Y.; Li, Y.; et al. Nonlinear optical modulation of MoS_2/black phosphorus/MoS_2 at 1550 nm. *Phys. B Condens. Matter* **2020**, *594*, 412364. [CrossRef]
108. Novoselov, K.S.; Mishchenko, A.; Carvalho, A.; Castro Neto, A.H. 2D materials and van der Waals heterostructures. *Science* **2016**, *353*, aac9439. [CrossRef]
109. Liu, Y.; Weiss, N.O.; Duan, X.; Cheng, H.-C.; Huang, Y.; Duan, X. Van der Waals heterostructures and devices. *Nat. Rev. Mater.* **2016**, *1*, 16042. [CrossRef]
110. Wang, Y.; Mu, H.; Li, X.; Yuan, J.; Chen, J.; Xiao, S.; Bao, Q.; Gao, Y.; He, J. Observation of large nonlinear responses in a graphene-Bi_2Te_3 heterostructure at a telecommunication wavelength. *Appl. Phys. Lett.* **2016**, *108*, 221901. [CrossRef]
111. Kumar, N.; Kumar, J.; Gerstenkorn, C.; Wang, R.; Chiu, H.-Y.; Smirl, A.L.; Zhao, H. Third harmonic generation in graphene and few-layer graphite films. *Phys. Rev. B* **2013**, *87*, 121406. [CrossRef]
112. Abdelwahab, I.; Grinblat, G.; Leng, K.; Li, Y.; Chi, X.; Rusydi, A.; Maier, S.A.; Loh, K.P. Highly Enhanced Third-Harmonic Generation in 2D Perovskites at Excitonic Resonances. *ACS Nano* **2018**, *12*, 644–650. [CrossRef]
113. Jiang, T.; Huang, D.; Cheng, J.; Fan, X.; Zhang, Z.; Shan, Y.; Yi, Y.; Dai, Y.; Shi, L.; Liu, K.; et al. Gate-tunable third-order nonlinear optical response of massless Dirac fermions in graphene. *Nat. Photonics* **2018**, *12*, 430–436. [CrossRef]
114. Rosa, H.G.; Ho, Y.W.; Verzhbitskiy, I.; Rodrigues, M.; Taniguchi, T.; Watanabe, K.; Eda, G.; Pereira, V.M.; Gomes, J.C.V. Characterization of the second- and third-harmonic optical susceptibilities of atomically thin tungsten diselenide. *Sci. Rep.* **2018**, *8*, 10035. [CrossRef]
115. Wang, R.; Chien, H.-C.; Kumar, J.; Kumar, N.; Chiu, H.-Y.; Zhao, H. Third-Harmonic Generation in Ultrathin Films of MoS_2. *ACS Appl. Mater. Interfaces* **2014**, *6*, 314–318. [CrossRef]
116. Youngblood, N.; Peng, R.; Nemilentsau, A.; Low, T.; Li, M. Layer-Tunable Third-Harmonic Generation in Multilayer Black Phosphorus. *ACS Photonics* **2017**, *4*, 8–14. [CrossRef]
117. Susoma, J.; Karvonen, L.; Säynätjoki, A.; Mehravar, S.; Norwood, R.A.; Peyghambarian, N.; Kieu, K.; Lipsanen, H.; Riikonen, J. Second and third harmonic generation in few-layer gallium telluride characterized by multiphoton microscopy. *Appl. Phys. Lett.* **2016**, *108*, 073103. [CrossRef]
118. Gu, T.; Petrone, N.; McMillan, J.F.; van der Zande, A.; Yu, M.; Lo, G.Q.; Kwong, D.L.; Hone, J.; Wong, C.W. Regenerative oscillation and four-wave mixing in graphene optoelectronics. *Nat. Photonics* **2012**, *6*, 554–559. [CrossRef]
119. Yang, Y.; Wu, J.; Xu, X.; Liang, Y.; Chu, S.T.; Little, B.E.; Morandotti, R.; Jia, B.; Moss, D.J. Invited Article: Enhanced four-wave mixing in waveguides integrated with graphene oxide. *APL Photonics* **2018**, *3*, 120803. [CrossRef]
120. Donnelly, C.; Tan, D.T. Ultra-large nonlinear parameter in graphene-silicon waveguide structures. *Opt. Express* **2014**, *22*, 22820–22830. [CrossRef]
121. Ji, M.; Cai, H.; Deng, L.; Huang, Y.; Huang, Q.; Xia, J.; Li, Z.; Yu, J.; Wang, Y. Enhanced parametric frequency conversion in a compact silicon-graphene microring resonator. *Opt. Express* **2015**, *23*, 18679–18685. [CrossRef] [PubMed]
122. Pasquazi, A.; Ahmad, R.; Rochette, M.; Lamont, M.; Little, B.E.; Chu, S.T.; Morandotti, R.; Moss, D.J. All-optical wavelength conversion in an integrated ring resonator. *Opt. Express* **2010**, *18*, 3858–3863. [CrossRef] [PubMed]
123. Xu, X.; Tan, M.; Corcoran, B.; Wu, J.; Boes, A.; Nguyen, T.G.; Chu, S.T.; Little, B.E.; Hicks, D.G.; Morandotti, R.; et al. 11 TOPS photonic convolutional accelerator for optical neural networks. *Nature* **2021**, *589*, 44–51. [CrossRef]
124. Pasquazi, A.; Peccianti, M.; Razzari, L.; Moss, D.J.; Coen, S.; Erkintalo, M.; Chembo, Y.K.; Hansson, T.; Wabnitz, S.; Del'Haye, P. Micro-combs: A novel generation of optical sources. *Phys. Rep.* **2018**, *729*, 1–81. [CrossRef]
125. Koos, C.; Vorreau, P.; Vallaitis, T.; Dumon, P.; Bogaerts, W.; Baets, R.; Esembeson, B.; Biaggio, I.; Michinobu, T.; Diederich, F.; et al. All-optical high-speed signal processing with silicon–organic hybrid slot waveguides. *Nat. Photonics* **2009**, *3*, 216–219. [CrossRef]
126. Ji, H.; Pu, M.; Hu, H.; Galili, M.; Oxenløwe, L.K.; Yvind, K.; Hvam, J.M.; Jeppesen, P. Optical Waveform Sampling and Error-Free Demultiplexing of 1.28 Tb/s Serial Data in a Nanoengineered Silicon Waveguide. *J. Lightwave Technol.* **2011**, *29*, 426–431. [CrossRef]

127. Jia, L.; Wu, J.; Zhang, Y.; Qu, Y.; Jia, B.; Chen, Z.; Moss, D.J. Fabrication Technologies for the On-Chip Integration of 2D Materials. *Small Methods* **2022**, *6*, 2101435. [CrossRef]
128. Qu, Y.; Wu, J.; Yang, Y.; Zhang, Y.; Liang, Y.; El Dirani, H.; Crochemore, R.; Demongodin, P.; Sciancalepore, C.; Grillet, C.; et al. Enhanced Four-Wave Mixing in Silicon Nitride Waveguides Integrated with 2D Layered Graphene Oxide Films. *Adv. Opt. Mater.* **2020**, *8*, 2001048. [CrossRef]
129. Qu, Y.; Wu, J.; Zhang, Y.; Jia, L.; Liang, Y.; Jia, B.; Moss, D.J. Analysis of Four-Wave Mixing in Silicon Nitride Waveguides Integrated with 2D Layered Graphene Oxide Films. *J. Lightwave Technol.* **2021**, *39*, 2902–2910. [CrossRef]
130. Alexander, K.; Savostianova, N.A.; Mikhailov, S.A.; Kuyken, B.; Van Thourhout, D. Electrically Tunable Optical Nonlinearities in Graphene-Covered SiN Waveguides Characterized by Four-Wave Mixing. *ACS Photonics* **2017**, *4*, 3039–3044. [CrossRef]
131. Feng, Q.; Cong, H.; Zhang, B.; Wei, W.; Liang, Y.; Fang, S.; Wang, T.; Zhang, J. Enhanced optical Kerr nonlinearity of graphene/Si hybrid waveguide. *Appl. Phys. Lett.* **2019**, *114*, 071104. [CrossRef]
132. Liu, L.; Xu, K.; Wan, X.; Xu, J.; Wong, C.Y.; Tsang, H.K. Enhanced optical Kerr nonlinearity of MoS_2 on silicon waveguides. *Photonics Res.* **2015**, *3*, 206–209. [CrossRef]
133. Guo, J.; Huang, D.; Zhang, Y.; Yao, H.; Wang, Y.; Zhang, F.; Wang, R.; Ge, Y.; Song, Y.; Guo, Z.; et al. 2D GeP as a Novel Broadband Nonlinear Optical Material for Ultrafast Photonics. *Laser Photonics Rev.* **2019**, *13*, 1900123. [CrossRef]
134. Jiang, X.; Zhang, L.; Liu, S.; Zhang, Y.; He, Z.; Li, W.; Zhang, F.; Shi, Y.; Lü, W.; Li, Y.; et al. Ultrathin Metal–Organic Framework: An Emerging Broadband Nonlinear Optical Material for Ultrafast Photonics. *Adv. Opt. Mater.* **2018**, *6*, 1800561. [CrossRef]
135. Vermeulen, N.; Castelló-Lurbe, D.; Cheng, J.; Pasternak, I.; Krajewska, A.; Ciuk, T.; Strupinski, W.; Thienpont, H.; Van Erps, J. Negative Kerr Nonlinearity of Graphene as seen via Chirped-Pulse-Pumped Self-Phase Modulation. *Phys. Rev. Appl.* **2016**, *6*, 044006. [CrossRef]
136. Ullah, K.; Meng, Y.; Shi, Y.; Wang, F. Harmonic Generation in Low-Dimensional Materials. *Adv. Opt. Mater.* **2022**, *10*, 2101860. [CrossRef]
137. Woodward, R.I.; Murray, R.T.; Phelan, C.F.; Oliveira, R.E.P.d.; Runcorn, T.H.; Kelleher, E.J.R.; Li, S.; Oliveira, E.C.d.; Fechine, G.J.M.; Eda, G.; et al. Characterization of the second- and third-order nonlinear optical susceptibilities of monolayer MoS_2 using multiphoton microscopy. *2D Mater.* **2017**, *4*, 011006. [CrossRef]
138. Autere, A.; Jussila, H.; Marini, A.; Saavedra, J.R.M.; Dai, Y.; Säynätjoki, A.; Karvonen, L.; Yang, H.; Amirsolaimani, B.; Norwood, R.A.; et al. Optical harmonic generation in monolayer group-VI transition metal dichalcogenides. *Phys. Rev. B* **2018**, *98*, 115426. [CrossRef]
139. Biswas, R.; Dandu, M.; Menon, S.; Jha, K.K.; Majumdar, K.; Raghunathan, V. Third-harmonic generation in multilayer Tin Diselenide under the influence of Fabry-Perot interference effects. *Opt. Express* **2019**, *27*, 28855–28865. [CrossRef]
140. Cui, Q.; Muniz, R.A.; Sipe, J.E.; Zhao, H. Strong and anisotropic third-harmonic generation in monolayer and multilayer ReS_2. *Phys. Rev. B* **2017**, *95*, 165406. [CrossRef]
141. Autere, A.; Ryder, C.R.; Säynätjoki, A.; Karvonen, L.; Amirsolaimani, B.; Norwood, R.A.; Peyghambarian, N.; Kieu, K.; Lipsanen, H.; Hersam, M.C.; et al. Rapid and Large-Area Characterization of Exfoliated Black Phosphorus Using Third-Harmonic Generation Microscopy. *J. Phys. Chem. Lett.* **2017**, *8*, 1343–1350. [CrossRef] [PubMed]